



**NAVAL  
POSTGRADUATE  
SCHOOL**

**MONTEREY, CALIFORNIA**

**THESIS**

**METASURFACE-BASED MEMS THZ-TO-IR  
FOCAL PLANE ARRAY**

by

Leroy E. Pimental

September 2018

Thesis Advisor:

Fabio D. Alves

Co-Advisor:

Gamani Karunasiri

**Approved for public release. Distribution is unlimited.**

**THIS PAGE INTENTIONALLY LEFT BLANK**

REPORT DOCUMENTATION PAGE			Form Approved OMB No. 0704-0188	
Public reporting burden for this collection of information is estimated to average 1 hour per response, including the time for reviewing instruction, searching existing data sources, gathering and maintaining the data needed, and completing and reviewing the collection of information. Send comments regarding this burden estimate or any other aspect of this collection of information, including suggestions for reducing this burden, to Washington headquarters Services, Directorate for Information Operations and Reports, 1215 Jefferson Davis Highway, Suite 1204, Arlington, VA 22202-4302, and to the Office of Management and Budget, Paperwork Reduction Project (0704-0188) Washington, DC 20503.				
<b>1. AGENCY USE ONLY</b> (Leave blank)		<b>2. REPORT DATE</b> September 2018	<b>3. REPORT TYPE AND DATES COVERED</b> Master's thesis	
<b>4. TITLE AND SUBTITLE</b> METASURFACE-BASED MEMS THZ-TO-IR FOCAL PLANE ARRAY			<b>5. FUNDING NUMBERS</b>	
<b>6. AUTHOR(S)</b> Leroy E. Pimental				
<b>7. PERFORMING ORGANIZATION NAME(S) AND ADDRESS(ES)</b> Naval Postgraduate School Monterey, CA 93943-5000			<b>8. PERFORMING ORGANIZATION REPORT NUMBER</b>	
<b>9. SPONSORING / MONITORING AGENCY NAME(S) AND ADDRESS(ES)</b> N/A			<b>10. SPONSORING / MONITORING AGENCY REPORT NUMBER</b>	
<b>11. SUPPLEMENTARY NOTES</b> The views expressed in this thesis are those of the author and do not reflect the official policy or position of the Department of Defense or the U.S. Government.				
<b>12a. DISTRIBUTION / AVAILABILITY STATEMENT</b> Approved for public release. Distribution is unlimited.			<b>12b. DISTRIBUTION CODE</b> A	
<b>13. ABSTRACT (maximum 200 words)</b> <p>Terahertz (THz) technology has gained momentum in recent years owing to special properties of THz waves being non-ionizing and at the same time being able to penetrate through non-metallic and non-polar materials. Nearly perfect THz absorption, optimized to particular THz quantum cascade laser (QCL) illumination sources, was achieved using metal-dielectric metasurfaces. The metasurfaces are composed of ultra-thin films of silicon oxide and aluminum, deposited on silicon substrates, and were fabricated using standard MEMS processes. The metasurface absorbers were structurally integrated onto an array of thermally insulated free-standing MEMS membranes that work as heat accumulators. The temperature of array is probed directly by a commercial thermal camera, translating the THz scene to infrared. The main characteristics such as spectral response, thermal time constant and sensitivity are controlled by the geometry and tuned by design according to the application demands. The results indicate great potential of using these THz sensors in real-time imaging applications. This thesis focuses on the development of the broadband IR emitter that will be probed by the IR camera. Several metamaterial broadband IR emitter geometries were evaluated and compared using finite element simulations.</p>				
<b>14. SUBJECT TERMS</b> terahertz, space, QCL, metamaterial, MEMS, infrared			<b>15. NUMBER OF PAGES</b> 75	
			<b>16. PRICE CODE</b>	
<b>17. SECURITY CLASSIFICATION OF REPORT</b> Unclassified	<b>18. SECURITY CLASSIFICATION OF THIS PAGE</b> Unclassified	<b>19. SECURITY CLASSIFICATION OF ABSTRACT</b> Unclassified	<b>20. LIMITATION OF ABSTRACT</b> UU	

THIS PAGE INTENTIONALLY LEFT BLANK

**Approved for public release. Distribution is unlimited.**

**METASURFACE-BASED MEMS THZ-TO-IR FOCAL PLANE ARRAY**

Leroy E. Pimental  
Lieutenant, United States Navy  
BSEE, University of Utah, 2010

Submitted in partial fulfillment of the  
requirements for the degree of

**MASTER OF SCIENCE IN APPLIED PHYSICS**

from the

**NAVAL POSTGRADUATE SCHOOL  
September 2018**

Approved by: Fabio D. Alves  
Advisor

Gamani Karunasiri  
Co-Advisor

Kevin B. Smith  
Chair, Department of Physics

THIS PAGE INTENTIONALLY LEFT BLANK

## **ABSTRACT**

Terahertz (THz) technology has gained momentum in recent years owing to special properties of THz waves being non-ionizing and at the same time being able to penetrate through non-metallic and non-polar materials. Nearly perfect THz absorption, optimized to particular THz quantum cascade laser (QCL) illumination sources, was achieved using metal-dielectric metasurfaces. The metasurfaces are composed of ultra-thin films of silicon oxide and aluminum, deposited on silicon substrates, and were fabricated using standard MEMS processes. The metasurface absorbers were structurally integrated onto an array of thermally insulated free-standing MEMS membranes that work as heat accumulators. The temperature of array is probed directly by a commercial thermal camera, translating the THz scene to infrared. The main characteristics such as spectral response, thermal time constant and sensitivity are controlled by the geometry and tuned by design according to the application demands. The results indicate great potential of using these THz sensors in real-time imaging applications. This thesis focuses on the development of the broadband IR emitter that will be probed by the IR camera. Several metamaterial broadband IR emitter geometries were evaluated and compared using finite element simulations.

THIS PAGE INTENTIONALLY LEFT BLANK

# TABLE OF CONTENTS

<b>I.</b>	<b>INTRODUCTION.....</b>	<b>1</b>
<b>II.</b>	<b>THZ-TO-IR BAND CONVERSION.....</b>	<b>5</b>
	<b>A. THZ ABSORBING METAMATERIAL .....</b>	<b>5</b>
	<b>B. THZ-TO-IR CONVERSION AND PERFORMANCE.....</b>	<b>7</b>
<b>III.</b>	<b>MEASUREMENT OF SENSOR CHARACTERISTICS .....</b>	<b>13</b>
	<b>A. EMISSIVITY MEASUREMENT .....</b>	<b>15</b>
	<b>B. SPEED OF OPERATION MEASUREMENT.....</b>	<b>16</b>
	<b>C. RESPONSIVITY MEASUREMENT.....</b>	<b>19</b>
<b>IV.</b>	<b>FINITE ELEMENT MODELING .....</b>	<b>23</b>
	<b>A. COMSOL HEAT TRANSFER IN SOLIDS AND SOLID MECHANICS MODEL.....</b>	<b>23</b>
	<b>B. COMSOL ELECTROMAGNETIC WAVES MODEL .....</b>	<b>26</b>
	<b>1. Unit Cell A: Sectional Asymmetric Structure [17] .....</b>	<b>28</b>
	<b>2. Unit Cell B: Square Resonators.....</b>	<b>37</b>
	<b>3. Increasing Dielectric Thickness Increases Thermal Capacitance .....</b>	<b>44</b>
<b>V.</b>	<b>CONCLUSION .....</b>	<b>49</b>
	<b>LIST OF REFERENCES.....</b>	<b>53</b>
	<b>INITIAL DISTRIBUTION LIST .....</b>	<b>55</b>

THIS PAGE INTENTIONALLY LEFT BLANK

## LIST OF FIGURES

Figure 1.	Electromagnetic Spectrum.....	1
Figure 2.	Schematic Diagram of THz-to-IR Imaging System.....	3
Figure 3.	Metamaterial Absorber. Source: [2]. .....	5
Figure 4.	Absorption vs. Frequency as S Varies. Source: [2]. .....	6
Figure 5.	Finite Element Simulation of Absorption of Metamaterial with Varying Dielectric Thickness. Source: [6].....	7
Figure 6.	MEMS THz-to-IR Converter. Source: [10]. .....	8
Figure 7.	Conversion Efficiency and Frequency of Operation for the THz to IR Sensor.....	12
Figure 8.	Measured Emissivities and Spectral Radiance of the 4.8 THz Metamaterial, and Oxidized Aluminum .....	14
Figure 9.	SEM Image of MEMs Sensor. Source: [10] .....	14
Figure 10.	Emissivity Measurement Experiment Setup.....	15
Figure 11.	Experimental Setup for Speed of Operation Measurements.....	17
Figure 12.	Screenshot from ResearchIR.....	18
Figure 13.	Speed of Operation Plot .....	18
Figure 14.	Setup for Measuring Incident Power .....	19
Figure 15.	Measured Incident Power, $\Phi_0$ , as a Function of QCL Power Supply Frequency.....	20
Figure 16.	Sensor Responsivity .....	21
Figure 17.	Conversion Efficiency and Frequency of Operation of the Fabricated Sensor.....	22
Figure 18.	COMSOL Thermal Model.....	24
Figure 19.	Steady State Temperature Distribution.....	25
Figure 20.	Temperature of the Sensor as the Incident Thermal Energy is Gated Between 0.1 Hz and 30 Hz .....	26

Figure 21.	Explored Unit Cell Geometries for Producing a Broad-Band Emitter .....	27
Figure 22.	COMSOL Electromagnetic Wave Model .....	28
Figure 23.	Unit Cell A Geometry .....	29
Figure 24.	Emissivity and Spectral Radiance of Unit Cell A as Resonator Segment Width is Varied .....	31
Figure 25.	Emissivity and Spectral Radiance of Unit Cell A as the Resonators are Scaled .....	32
Figure 26.	Emissivity and Spectral Radiance of Unit Cell A as the Dielectric Thickness is Varied .....	33
Figure 27.	Emissivity and Spectral Radiance for an Optimized Geometry for Unit Cell A .....	34
Figure 28.	Conversion Efficiency and Frequency of Operation for Unit Cell A .....	35
Figure 29.	Emissivity as Dielectric Thickness is Varied for Unit Cell A for a Frequency Dependent Refractive Index and a Constant Refractive Index .....	36
Figure 30.	Emissivity and Spectral Radiance of Unit Cell A as Notches are Removed .....	37
Figure 31.	Unit Cell B Geometry .....	38
Figure 32.	and Spectral Radiance of Unit Cell B as the as the Size of $S_1$ is Varied .....	39
Figure 33.	Emissivity and Spectral Radiance of Unit Cell B as the as the Size of $S_3$ is Varied .....	40
Figure 34.	Emissivity and Spectral Radiance of Unit Cell B as Dielectric Thickness is Varied .....	41
Figure 35.	Emissivity and Spectral Radiance for an Optimized Geometry for Unit Cell B .....	42
Figure 36.	Conversion Efficiency and speed of Operation for Unit Cell B .....	43
Figure 37.	Emissivity as the Size of $S_3$ is Varied for Unit Cell B for a Frequency Dependent Refractive Index and a Constant Refractive Index .....	45

Figure 38. Emissivity and Spectral Radiance of the Simulated and Fabricated Unit Cell B Geometry .....46

Figure 39. Conversion Efficiency of Unit Cell B vs. a Blackbody Emitter .....48

THIS PAGE INTENTIONALLY LEFT BLANK

## LIST OF TABLES

Table 1.	Geometric Dimensions of COMSOL Thermal 3D Model.....	23
Table 2.	Material Properties Used in COMSOL Simulation.....	25
Table 3.	Geometries Used in Unit Cell A Simulations.....	30
Table 4.	Geometries Used in Unit Cell B Simulations .....	38
Table 5.	Summary of Results For Unit Cells A, B, and C.....	47

THIS PAGE INTENTIONALLY LEFT BLANK

## **LIST OF ACRONYMS AND ABBREVIATIONS**

Al	Aluminum
FE	Finite Element
FPA	Focal Plane Array
FSS	Frequency Selective Surface
FTIR	Fourier Transform Infrared Spectrometer
IR	Infrared
MEMS	Microelectromechanical Systems
NPS	Naval Postgraduate School
PML	Perfectly Matched Layer
PSD	Position Sensitive Photodetector
QCL	Quantum Cascade Laser
SEM	Scanning Electron Microscope
SRL	Sensors Research Lab

THIS PAGE INTENTIONALLY LEFT BLANK

## **ACKNOWLEDGMENTS**

I would like to thank the Physics Department and professors for their mentorship and for a quality education. Their unwavering support and dedication made my time at NPS a pleasurable and rich experience. I would like to especially thank my advisors, Dr. Fabio Alves and Dr. Gamani Karunasiri. Their constant push to make me a better student and physicist has taught me things that I will carry with me for life. I would also like to thank my wonderful wife, Jessica. My successful graduate education would not have been possible without her dedication and support.

THIS PAGE INTENTIONALLY LEFT BLANK

## I. INTRODUCTION

The electromagnetic spectrum, reported in Figure 1, has been largely explored for potential applications. For example, longer wavelength radio and microwave frequencies are used for wireless communications such as radio and television transmissions, wireless data, and cellphones. This spectrum is also utilized for RADAR and microwave ovens. The infrared spectrum is used for imaging, fiber optic communication, and certain remote controls. The ultraviolet spectrum is used for photolithography, resin curing, and in suntan booths. X-rays and gamma rays are used for various types of imaging in the medical, security, and science communities. The terahertz band sits between the microwave and infrared band at 100 GHz–10 THz, and exhibits such distinct characteristics as penetrating through non-metallic objects and non-ionizing. Nevertheless, the THz band has been unexplored until recently. New and more powerful sources, and more efficient sensors are on the horizon. Particularly due to advances in metamaterials, THz sensing has evolved significantly over recent years.

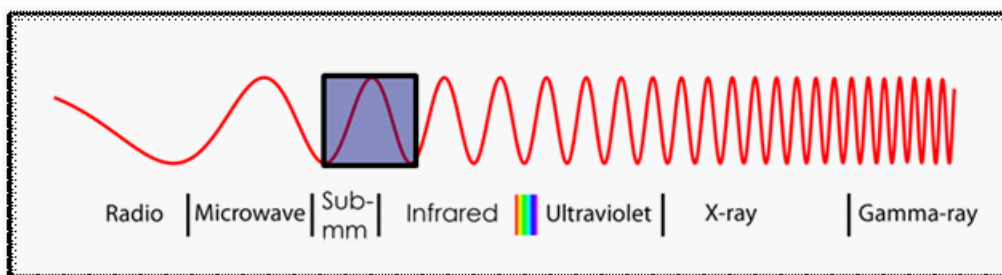


Diagram showing the electromagnetic spectrum with the THz band boxed in blue.

Figure 1. Electromagnetic Spectrum.

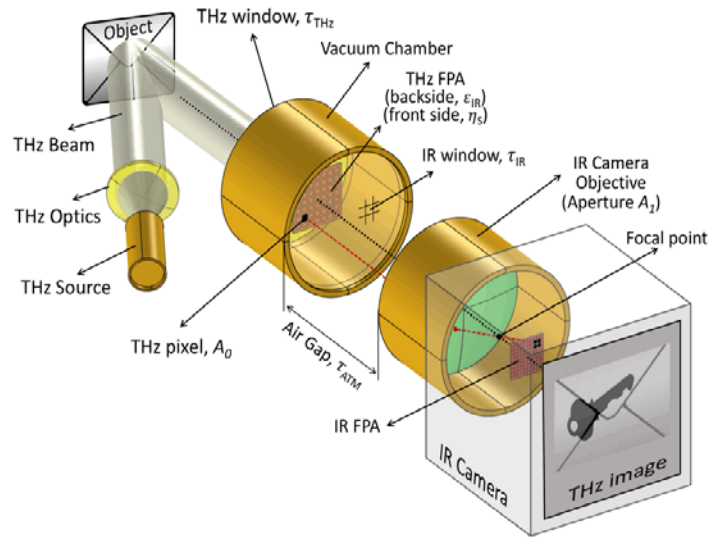
Tao et al. [1]. demonstrated the possibility of using microelectromechanical systems (MEMS) technology to fabricate a terahertz imaging sensor. Tao designed and fabricated a bi-material cantilever pixel for detection of 95 GHz and 693 GHz frequencies. Each pixel was fabricated using MEMS by depositing 500 nm of SiN<sub>x</sub> on a silicon substrate, and then depositing and etching a gold (Au) split ring resonator and

readout reflectors. Each pixel heats up, as it absorbs THz radiation, and deflects due to the bi-material properties of the legs attached to it. The deflection is measured using a position sensitive photodetector (PSD). Using this method, Tao was able to achieve an approximate 40% absorption, which could be improved by using a perfect absorption metamaterial geometry. Despite the high sensitivity that can be achieved with bi-material configurations [2], in practice some limitations can be identified. For example, Tao reported that the optical readout system was the main contributor to noise, and that it was sensitive to environmental vibration. Optical readouts for focal plane arrays (FPA), which are not achievable with PSDs, are complex and relatively difficult to implement [3]. Furthermore, cantilever structures are prone to residual stresses that deform after fabrication increasing the difficulty of using an optical readout system.

A promising alternative to overcome the limitations of the bi-material pixel is to directly read the heat generated by the absorption of the terahertz energy Kuzentsov et al. [4]. proposed a sub-terahertz (0.3 THz) sensor that converts THz to infrared (IR) radiation. Kuzentsov's sensor was composed of a polarization-sensitive and frequency-selective surface (FSS), composed of a split-ring resonator array on top of a layer of polypropylene dielectric substrate. The backside of the sensor was composed of an IR-emissive layer, made of an unspecified material with an aluminum ground plane separating the IR-emissive backside from the FSS front side. In this design, the front side FSS would absorb co-polar THz radiation at a resonant frequency. The absorbed energy is stored as heat, which is then radiated by the IR emissive layer. Because Kuzentsov utilized a split-ring resonator as the metamaterial THz absorber, the sensor is polarization sensitive. He was able to achieve near perfect absorption at 0.30 THz only when the incoming THz signal was co-polarized and no absorption at 0.30 THz when the incoming signal was cross-polarized. There is no discussion on conversion efficiency, but because each "pixel" shares a common dielectric and ground plane, and is not thermally isolated, cross-talk between pixels is expected.

We conceived our sensor based on the ideas of Kuzentsov by thermally isolating the pixels, using a perfect or near perfect planar metamaterial absorber that is polarization independent for THz absorption. In addition, to maximize energy emitted in the IR

camera's sensitivity band, another metamaterial layer is used with selective emissivity in the IR band of the camera. Figure 2 shows a schematic diagram of the proposed imaging system. This figure shows a THz source, in our experiments, a 4.75 THz quantum cascade laser (QCL), illuminating an object (a metallic key inside an envelope). The reflected THz radiation reaches the THz-to-IR FPA, which is inside a vacuum chamber sealed by two transmissive windows. The THz window, with transmissivity of  $\tau_{THz}$ , allows THz to pass through while blocking IR. The IR side window, with transmissivity  $\tau_{IR}$ , allows the heat from the backside of the FPA to radiate towards the IR camera objective through an air gap with transmissivity  $\tau_{atm}$ . Each pixel, with an area of  $A_0$ , absorbs the THz radiation with an absorptivity of  $\eta_s \equiv \varepsilon_{THz}$ . This absorbed radiation is thermally stored and emitted on the IR side with an emissivity of  $\varepsilon_{IR}$ . The signal is then captured by the IR camera aperture, with an area of  $A_1$ , and processed by the IR camera. The transmissivity of the IR camera lens and optics, as well as the spectral responsivity of the camera, is combined into a single parameter,  $\tau_{IR-camera}$ . The sensor/FPA are designed based on the concept shown in Figure 2.



A schematic diagram depicting an object, a metallic key concealed in an envelope, illuminated by a THz source, with the IR camera capturing the converted IR image. The dotted red line depicts an excited THz pixel being mapped to pixels on the IR focal plane array (FPA). The Greek letters  $\tau$ ,  $\eta$  and  $\varepsilon$  represent transmissivity, absorptivity and emissivity, respectively.

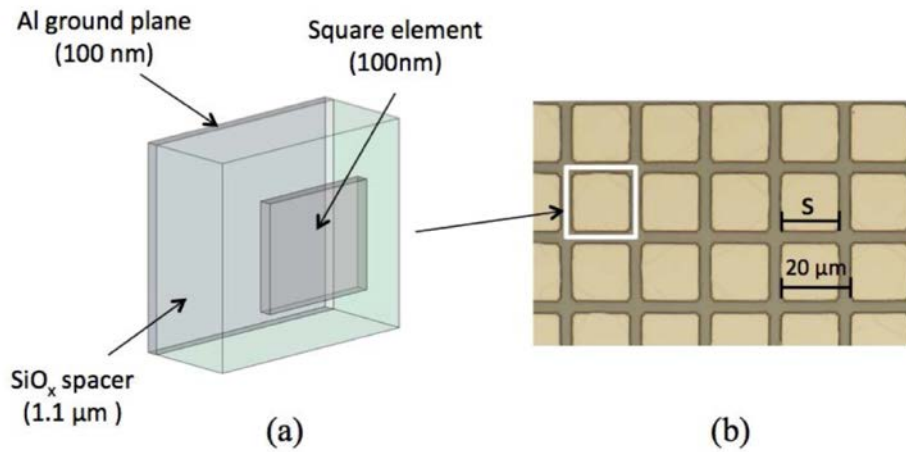
Figure 2. Schematic Diagram of THz-to-IR Imaging System.

Earlier work done in the Sensors Research Lab (SRL) at the Naval Postgraduate School (NPS) includes a variety of approaches in THz sensing and imaging. This research includes the use of an uncooled microbolometer camera to detect THz from a QCL source [3], [5]. This research evolved into exploring the use of metamaterials as a perfect THz absorber, and integrating the it into a MEMS bi-material THz FPA [6], [7], [8], [9]. Due to the disadvantages of optical readout systems employed in bi-material sensors, a sensor using direct conversion of THz to IR, as shown in Figure 2, is now being explored [10], [11], [12]. SRL has already established the structure and concept of the THz-to-IR sensor and how to get near perfect THz absorption. What has not been established is how to measure sensor performance and how to design a broadband selective IR emissive layer for the sensor in order to improve performance. A THz-to-IR FPA has been fabricated by our group, but the backside of the sensor is composed of the same THz metamaterial as the front side. This thesis will focus on defining performance parameters, taking measurements on the existing sensors, and simulating/designing an IR emitter, which will be used for the backside of the sensor. This thesis will start off describing prior work SRL has done on designing a THz metamaterial absorber. These concepts have been well-established and will be important in establishing a design for a broadband IR metamaterial emitter. From there, an explanation on the THz-to-IR conversion process with an in-depth explanation on how conversion efficiency and frequency of operation is used to determine sensor performance. The measurements section will then cover lab experiments conducted in order to validate our finite element (FE) model. The thermal time constant measurements along with emissivity and responsivity measurements will be discussed. The simulation chapter has an in-depth discussion on different geometries explored in developing an IR broadband emitter. The conclusion will summarize the results and explain the next steps in furthering the development of a THz-to-IR sensor.

## II. THZ-TO-IR BAND CONVERSION

### A. THZ ABSORBING METAMATERIAL

The use of metamaterial is a very attractive option for THz sensors. The challenge is to design a metamaterial that is a perfect absorber for a specific narrow frequency band, regardless of polarization. Our research group has developed a metamaterial design using a periodic array of aluminum (Al) squares on a  $\text{SiO}_x$  spacer with an Al ground plane as shown in Figure 3 [2]. References [2], [6], and [7] show that as the square size,  $S$ , varies, the absorption resonant frequency also changes. Figure 3 shows the geometry of the test metamaterial. It consisted of a 100 nm Al ground plane with a  $1.1 \mu\text{m}$   $\text{SiO}_x$  spacer and 100 nm Al square elements. The period was kept at a constant  $20 \mu\text{m}$ , and the square size varied between  $16 \mu\text{m}$  and  $18 \mu\text{m}$ .

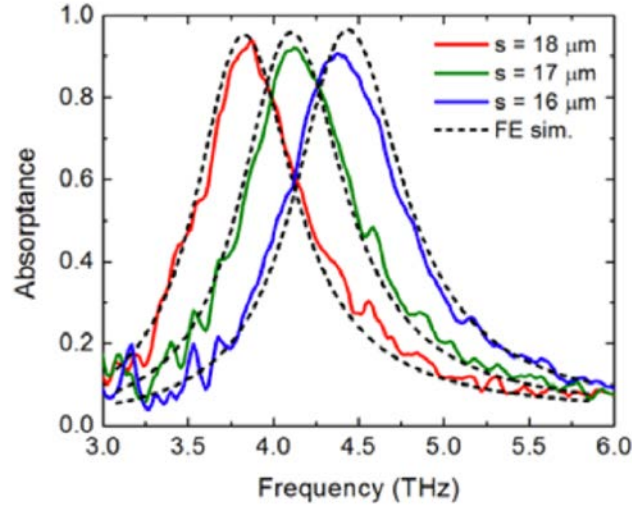


(a) Metamaterial unit cell design and (b) periodic array, with a period of  $20 \mu\text{m}$ , of metamaterial that was tested.  $S$  is varied while maintaining a constant period.

Figure 3. Metamaterial Absorber. Source: [2].

Fourier transform infrared spectrometer (FTIR) was used to measure absorption as function of frequency. Three metamaterials were fabricated with square sizes  $16 \mu\text{m}$ ,  $17 \mu\text{m}$ , and  $18 \mu\text{m}$ ; all with a period of  $20 \mu\text{m}$ ,  $1.1 \mu\text{m}$  dielectric spacer and 100 nm ground plane. Figure 4 compares the FE simulation to measured absorption as square size

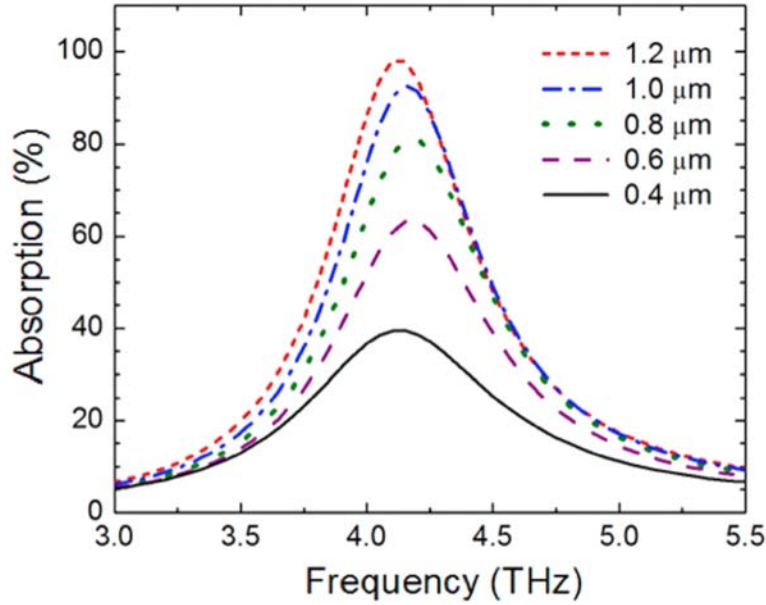
is varied. A It has been proven that peak resonance is proportional to the inverse of the square size [7].



Comparison between measured (solid line) and simulated (dash line) absorption of three different metamaterials with different square sizes.

Figure 4. Absorption vs. Frequency as S Varies. Source: [2].

Our group has also found by FE modeling that the absorption of metamaterials can be controlled by varying dielectric thickness as shown in Figure 5 [6]. The metamaterial used consists of an Al ground plane  $95 \mu m$  thick, Al squares with  $S = 16.3 \mu m$ , a period of  $21 \mu m$ , with the  $SiO_2$  spacer varying between  $0.4 \mu m$  and  $1.2 \mu m$ . Figure 5 shows that absorption increases as the dielectric spacer thickness increases. It is important to note that once the dielectric layer thickness increased beyond about  $1.4 \mu m$ , absorption starts decreasing. Using these two concepts, adjusting square size to tune resonant absorption, and adjusting dielectric thickness to adjust percent absorption, it is possible to produce a THz narrow-band, perfect absorber. As discussed later in this thesis, we can also apply these concepts to produce a metamaterial that emits IR in the specific band that matches the sensitivity of our IR camera.

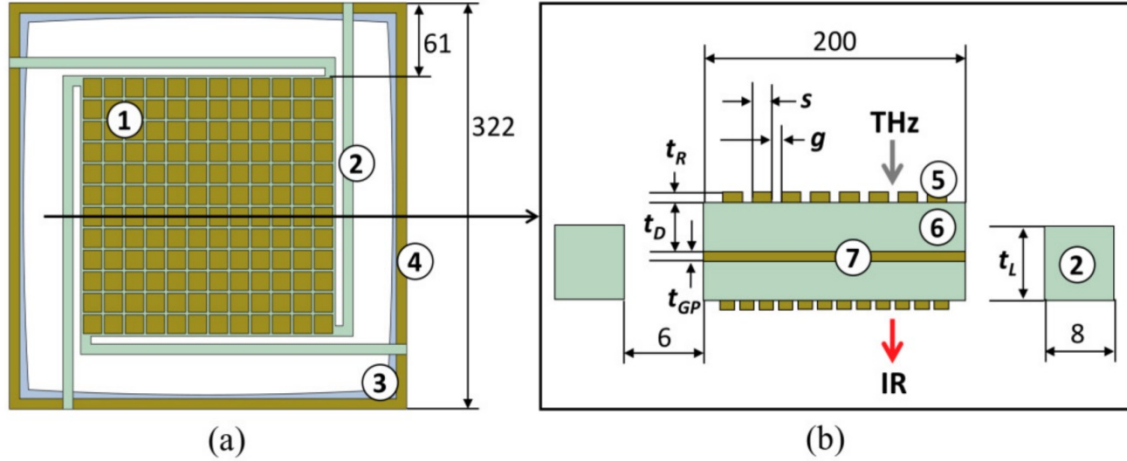


Comparison of percent absorption of metamaterial with constant square size,  $16.3 \mu\text{m}$ , period,  $21 \mu\text{m}$  and varying  $\text{SiO}_2$  dielectric thickness.

Figure 5. Finite Element Simulation of Absorption of Metamaterial with Varying Dielectric Thickness. Source: [6].

## B. THZ-TO-IR CONVERSION AND PERFORMANCE

The design goal is to produce a THz-to-IR pixel that maximizes absorption in the band we are interested in, and has high emissivity in the band of our camera. Figure 6 shows the proposed design for the metamaterial THz-to-IR pixel. Each pixel is composed of a double-sided metamaterial. The front side absorbs the incoming THz radiation, causing the pixel to increase in temperature from  $T_0$  to  $T_0 + \Delta T$ . The heat that is stored in the pixel is isolated from the rest of the sensor by four symmetrically-placed thermal-isolating beams. In order to get a high conversion efficiency, the beams will need to be designed to minimize thermal conduction. This will allow more energy to be radiate by the metamaterial emitter on the backside of the pixel.



(a) top view showing one pixel of the converter. All units are in  $\mu m$ . (1) is the metamaterial absorber. (2) is thermal isolating legs. (3) is the substrate frame. (4) is the aluminum frame which acts as the heatsink. (b) cross-section view of one pixel of the converter. (5) aluminum resonators. (6) dielectric spaces. (7) aluminum ground plane.  $t_R$ ,  $t_D$ ,  $t_{GP}$  and  $t_L$  represent the thickness of the resonators, dielectric, ground plane, and thermal-isolating legs, respectively.

Figure 6. MEMS THz-to-IR Converter. Source: [10].

To aid in the design of the thermal converter, measurable parameters must be established. The main parameters used for measuring performance are conversion efficiency,  $eff$ , frequency of operation,  $f_{OP}$  [Hz]. which is related to the thermal time constant,  $f_{OP} = \frac{1}{2\pi\tau_{th}}$ , and responsivity,  $R$ . Conversion efficiency considers how sensitive the sensor is in the THz band and how selective it is in the IR band. To define these parameters and establish their co-dependencies, a step-by-step analysis of the conversion process will be evaluated.

As the incoming THz flux,  $\Phi_0$ , is absorbed by the sensor, several things happen. Some of this energy will cause the sensor to increase in temperature by  $\Delta T$ , and some of the energy will be lost. There are three ways that energy will be lost: Conduction through the thermal isolating legs; convection, which will be neglected since the sensor will be operating in near vacuum; and radiation. Thermal conduction and radiation will be lumped into a single parameter  $G_{th}$  [W/K], which represents the change in thermal flux per change in temperature. The THz absorption process can be represented by the heat balance equation (1):

$$C_{th} \frac{d(\Delta T)}{dt} + G_{th} \Delta T = \eta_S \Delta \Phi_0, \quad (1)$$

where  $\eta_S$  is the absorptivity of the front side of the sensor and  $\eta_S \Delta \Phi_0$  represents the energy flux being absorbed by the sensor.  $C_{th}$  [J/K] represents the thermal capacitance of the sensor, and  $C_{th} \frac{d(\Delta T)}{dt}$  represents energy flux stored in the sensor as heat.  $G_{th} \Delta T$  represents the energy flux being lost due to thermal conduction,  $\Phi_C$ , and total radiation flux,  $\Phi_{vR}$ , and therefore

$$G_{th} = \frac{d(\Phi_{vR} + \Phi_C)}{dT}. \quad (2)$$

The thermal conductive flux,  $\Phi_C$ , represents the thermal flux through the thermal insulating legs and therefore can be calculated by

$$\Phi_C = 4 \frac{\kappa_{th} A_C \Delta T}{L_{leg}}, \quad (3)$$

where  $\kappa_{th}$  is the thermal conduction insulating leg material, the multiplication factor, 4, is to account for the four insulating legs,  $A_C$  is the cross-sectional area of the insulating legs,  $\Delta T$  is the temperature difference between the sensor and the frame substrate, and  $L_{leg}$  is the linear length of the of one insulating legs.

Since the sensor is made of different materials, the total thermal capacitance can be calculated using the following:

$$C_{th} = \sum_n c_n A_0 \rho_n d_n, \quad (4)$$

where  $n$  is an index representing the layer,  $c_n$  [J/(gK)], is the specific heat capacity for the layer,  $A_0$  is the surface area of the e element,  $\rho_n$  is the density of the layer and  $d_n$  is the thickness of the layer.

The total radiation flux of the sensor  $\Phi_{vR}$  represents the radiation flux from both the THz side and the IR side, and can be calculated by

$$\Phi_{vR} = A_0 \pi \int_0^\infty \varepsilon_{THZ}(\nu) L_{0\nu} d\nu + A_0 \pi \int_0^\infty \varepsilon_{IR}(\nu) L_{0\nu} d\nu, \quad (5)$$

where  $\varepsilon_{THZ}$  and  $\varepsilon_{IR}$  are the emissivities of the THz metamaterial side and IR metamaterial side, respectively.  $L_{0\nu}$  [W/(m<sup>2</sup>sr)] is the spectral radiance which is given by

$$L_{0v} = \left(\frac{2h\nu^3}{c^2}\right) \left(\frac{1}{\exp\left(\frac{h\nu}{kT}\right)-1}\right), \quad (6)$$

where  $h$  is Plank's constant,  $c$  is the speed of light, and  $k$  is Boltzmann's constant and  $T$  is the temperature of the sensing element in Kelvin.

The responsivity of the sensor is defined by the change in temperature of the sensing element per unit of incident flux,  $R = \frac{\Delta T}{\Delta \Phi_0}$ . Assuming  $\Delta \Phi_0$  is sinusoidal, equation (1) can be solved for  $\Delta T$  as

$$\Delta T = \frac{\eta_S \Delta \Phi_0}{G_{th} \sqrt{1 + (\omega \tau_{th})^2}}. \quad (7)$$

For  $\omega \ll 1/\tau_{th}$   $\Delta T$  can be approximated by

$$\Delta T \approx \frac{\eta_S \Delta \Phi_0}{G_{th}} \quad (8)$$

Therefore, responsivity can be represented by

$$R = \frac{\eta_S}{G_{th}} [K/\mu W]. \quad (9)$$

This shows that there is a trade-off between responsivity and speed of operation of the sensor. The thermal time constant is given by  $\tau_{th} = C_{th}/G_{th}$ ; therefore, the frequency of operation is given by:

$$f_{OP} = \frac{G_{th}}{2\pi C_{th}} \quad (10)$$

Decreasing thermal conductance,  $G_{th}$ , will increase responsivity, but will decrease the speed of operation of the sensor. It might be tempting to compensate by decreasing thermal capacitance,  $C_{th}$ , to mitigate the loss in the speed of operation. Nevertheless, to decrease the thermal capacitance would require decreasing the dielectric thickness, and as previously explained in Section A, this will decrease absorption and subsequently decrease  $\eta_S$ , and hence decrease responsivity. An optimization process should be used to obtain the desired response for each application.

Using responsivity as a metric for sensor performance can be deceptive. For example, looking at equations (5), (2), and (9) decreasing the emissivity of the backside

of the sensor,  $\epsilon_{IR}$ , while keeping the incident flux,  $\Delta\Phi_0$ , constant would increase responsivity, and therefore would suggest an increase in sensor performance. But, as  $\epsilon_{IR}$  decreases, the radiative flux coming out of the sensor also decreases. Since the purpose of the sensor is to emit IR that the camera can detect, this would decrease the system performance. Instead of using responsivity, conversion efficiency will be used as a metric of system performance. We define conversion efficiency as the change in IR radiated flux within the spectral band of the IR camera,  $\Delta\Phi_{vIR}$ , over the change in incident flux,  $\Delta\Phi_0$ . Assuming the sensor acts as a Lambertian radiator,  $\Delta\Phi_{vIR}$  can be calculated by

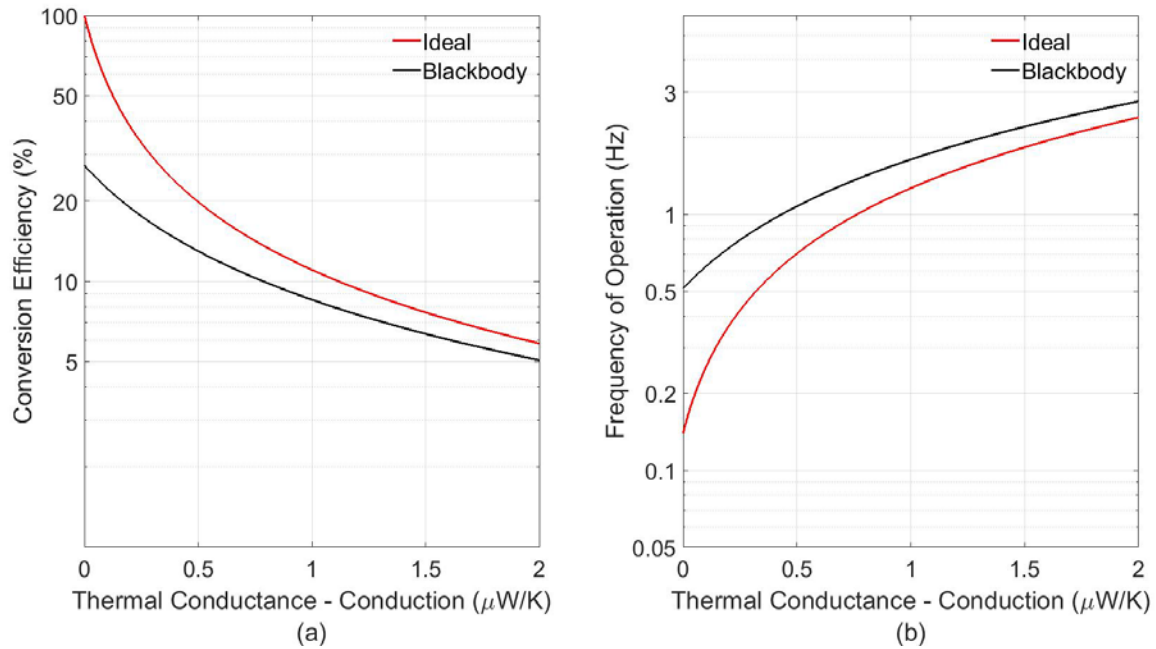
$$\Delta\Phi_{vIR} = A_0\pi\left(\int_{\nu_1}^{\nu_2} \epsilon_{IR}(\nu)L_{0\nu}(T)d\nu - \int_{\nu_1}^{\nu_2} \epsilon_{IR}(\nu)L_{0\nu}(T_0)d\nu\right), \quad (11)$$

where  $A_0$  is the surface area of the sensor. The multiplication factor  $\pi$  represents the solid angle of the projected radiation of the backside of the sensor.  $\epsilon_{IR}$  is the emissivity of the IR/back side of the sensor.  $T_0$  is the initial temperature of the sensor and  $T$  is the final temperature of the sensor. Therefore, conversion efficiency can be represented by

$$eff = \frac{A_0\pi\left(\int_{\nu_1}^{\nu_2} \epsilon_{IR}(\nu)L_{0\nu}(T)d\nu - \int_{\nu_1}^{\nu_2} \epsilon_{IR}(\nu)L_{0\nu}(T_0)d\nu\right)}{\Delta\Phi_0}. \quad (12)$$

This equation shows that as the thermal conduction through the thermal insulating legs decreases, efficiency increases. This is because for a given change in  $\Delta\Phi_0$  more of the energy is now being radiated in the IR instead of being lost due to conduction. Max efficiency is reached when emissivity of the backside,  $\epsilon_{IR}$ , of the sensor is one for the band of the IR camera, and zero otherwise; when the absorptivity of the front side,  $\eta_s$ , is one for the band of the THz source, and zero otherwise, and when thermal conduction,  $G_{cond}$ , is zero. Figure 7(a) shows a plot of the conversion efficiency of this ideal sensor as thermal conduction is varied. To compare, the conversion efficiency is plotted as if the sensor acts as a perfect blackbody ( $\epsilon_{IR} = \epsilon_{THz} = 1$ ). To illustrate the inverse relationship of conversion efficiency and speed of the sensor, the frequency of operation is plotted in Figure 3 (b). Calculations for Figure 3 are for room temperature,  $T_0 = 300 K$ , with a  $\Delta T = 1 K$ , element surface area of  $A_0 = 200 \mu m \times 200 \mu m$  and a dielectric thickness of  $d = 2.2 \mu m$ .

Figure 7(a) shows how quickly conversion efficiency decreases as thermal conduction increases. As little as  $0.5\mu\text{W/K}$  thermal conductance reduces conversion efficiency by 80%, but only increases speed of operation by less than 1 Hz. These figures of merit of sensor performance will be important when considering design parameters. The next chapter describes experimental measurements of a previously fabricated THz-to-IR converter. The sensor was fabricated to prove the concept of metamaterial-based band conversion and to allow the development of experimental methods to access conversion efficiency among other performance characteristics.

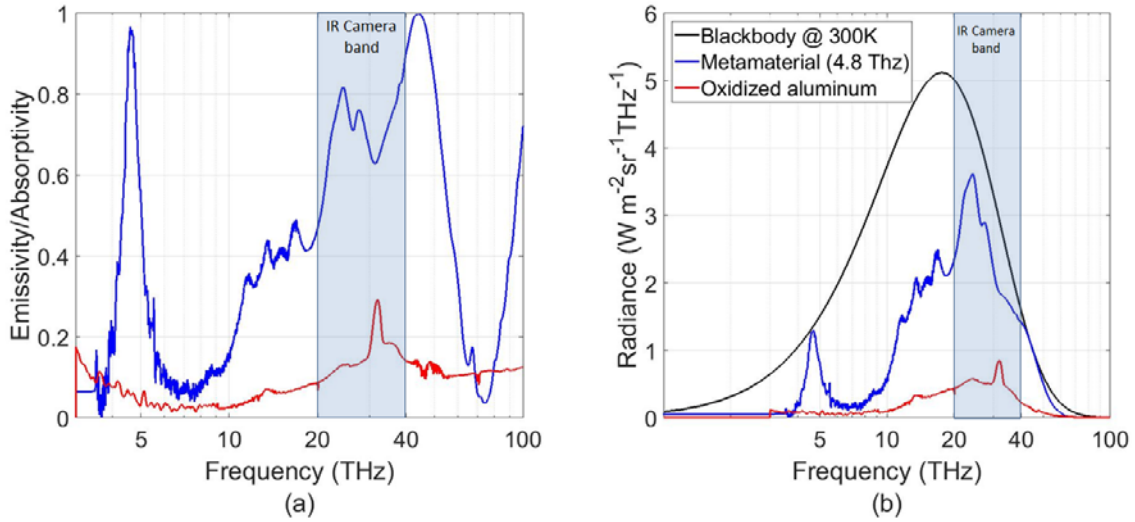


Effects of thermal conduction,  $G_{cond}$ , on (a) conversion efficiency and on (b) the frequency of operation for ideally selective metamaterial (red line), and on a sensor with the absorption and emissivity of a blackbody (black line).

Figure 7. Conversion Efficiency and Frequency of Operation for the THz to IR Sensor

### III. MEASUREMENT OF SENSOR CHARACTERISTICS

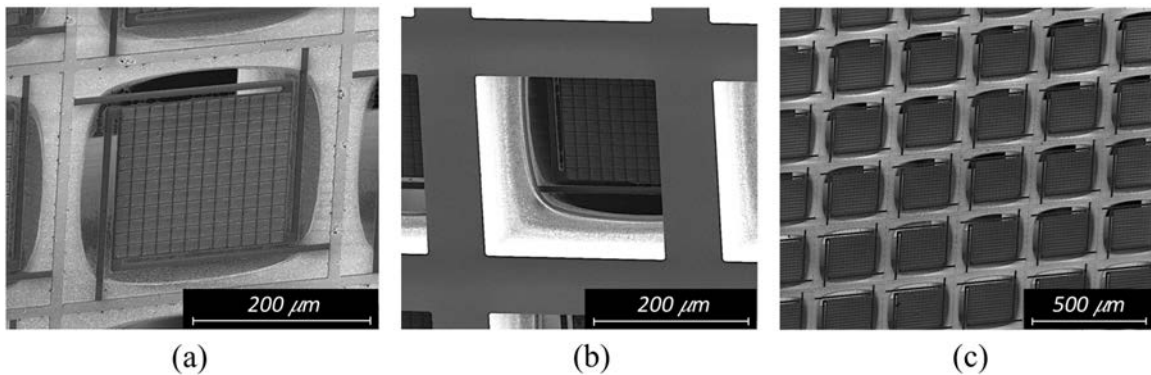
As a proof of concept, a sensor was fabricated using common MEMS fabrication techniques. The front side of the sensor consisted of metamaterial tuned to 4.75 THz, the frequency of the QCL used in our experiments. The backside of the sensor consisted of the same metamaterial used for the front side; this simplified the fabrication process. The sensor's geometry is as shown in Figure 6. Each pixel is 200  $\mu\text{m}$  by 200  $\mu\text{m}$ . Both sets of resonators are composed of 90 nm thick Al ( $t_R$ ) with resonator sizes,  $S$ , equal to 14.5  $\mu\text{m}$  and resonator gap,  $g$ , equal to 2  $\mu\text{m}$ . Both dielectric spacers are composed of 1.1  $\mu\text{m}$  ( $t_D$ ) of  $\text{SiO}_2$  making the thermal isolating leg thickness,  $t_L$ , 2.2  $\mu\text{m}$ . The ground plane is composed of 90 nm ( $t_{GP}$ ) of Al. Figure 8 (a) shows the Absorption/Emissivity of the metamaterial in the THz and IR bands using an naturally oxidized Al layer as reference. Figure 8 (b) shows the spectral radiance at 300 K. As can be seen, the metamaterial is almost a perfect match in the THz range (narrow response with the peak at 4.8 THz), however it is not ideal in the IR range. As it can be seen in Figure 8, emissivity of the metamaterial film in IR range is still better than oxidized aluminum. Figure 9 shows a magnified picture of the sensor using a scanning electron microscope (SEM) [10].



Plots comparing measured emissivity and spectral radiance of a metamaterial (tuned to 4.8 THz) with that of oxidized aluminum. The shaded region represents the sensitivity band of the IR camera.

Figure 8. Measured Emissivities and Spectral Radiance of the 4.8 THz Metamaterial, and Oxidized Aluminum

Measurements from the fabricated sensor were used to refine our FE simulations. As described in the next section, an average emissivity over the band of the IR camera was measured and used to refine the thermal FE model. The speed of operation was also measured and used to refine our simulation's thermal conductance parameter.



Magnified micrograph of the (a) front side, (b) back side, and (c) an expanded view of the fabricated sensor used in the experiments outlined in this paper. Images taken using a SEM using a beam power of 2 kV. Source: [10].

Figure 9. SEM Image of MEMS Sensor. Source: [10].

## A. EMISSIVITY MEASUREMENT

In order to measure the emissivity of the sensor, the sensor was attached to a heater, where the temperature would be precisely controlled. Figure 10 is a schematic diagram of the setup used to measure the average emissivity of the metamaterial layer of the sensor in the IR range of the FLIR camera. The temperature was set to 35° C and the heater and sensor were allowed to reach a steady-state. A FLIR T130sc IR camera, controlled by the software ResearchIR [13], was used to take the measurement. ResearchIR allowed setting a region of interest in the middle of the THz sensor's pixel, where the temperature was measured. The emissivity setting in ResearchIR was adjusted until the temperature given by the IR camera was the same as the actual temperature imposed by the temperature controller, and then recorded as the average emissivity.

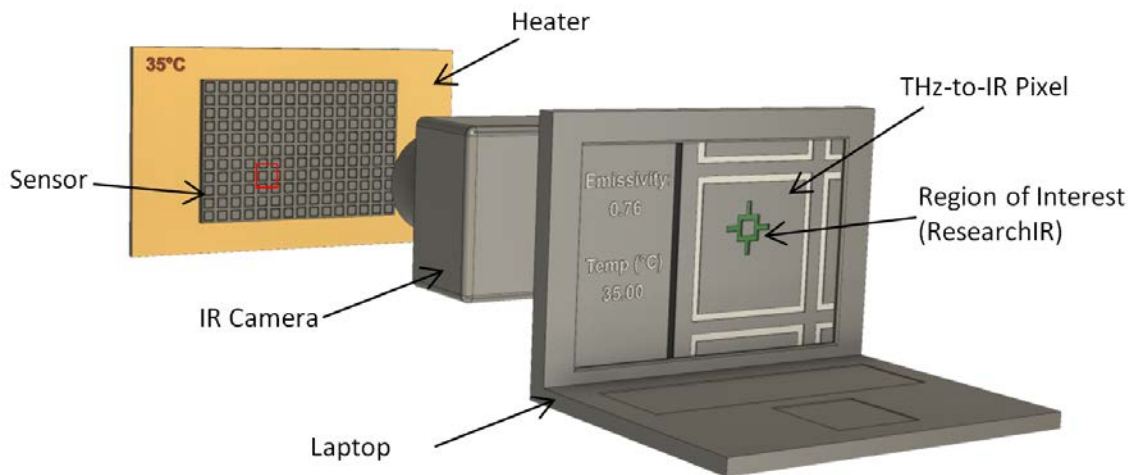


Diagram of the emissivity measurement setup. The sensor is attached to the heater and the FLIR T1030sc IR camera is focused on the sensor. The camera was controlled and measurements taken with the program ResearchIR, which was loaded on a laptop.

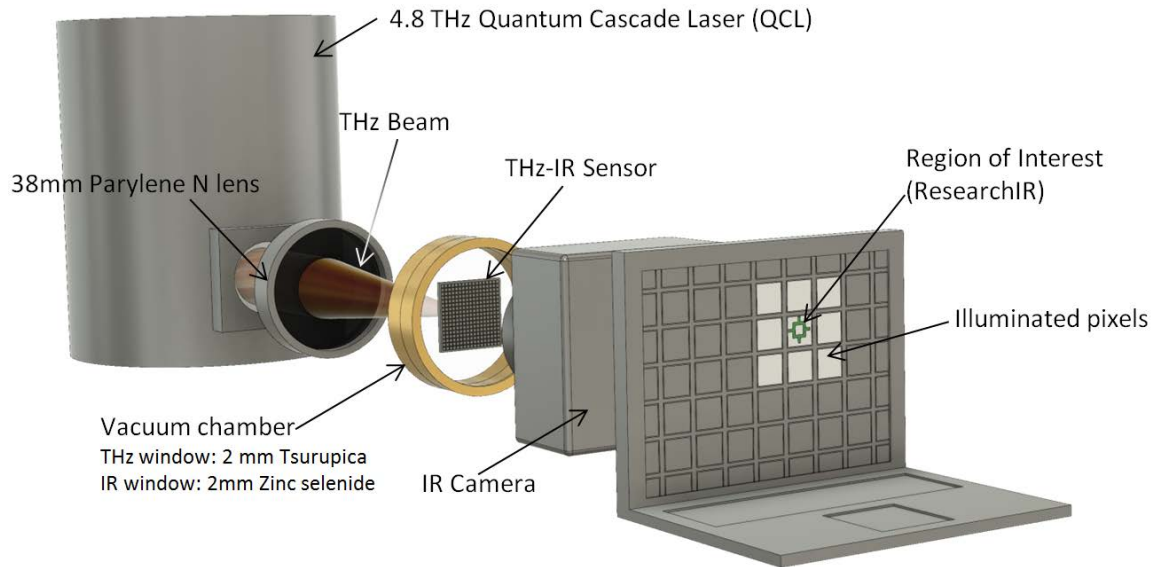
Figure 10. Emissivity Measurement Experiment Setup

An emissivity of 0.76 was measured; this emissivity represents the average emissivity of our sensor over the band of the camera, 7.5–14  $\mu\text{m}$  [14]. We then used this measurement to set the emissivity of our sensor in our thermal FE model. An accurate

emissivity value in our thermal model is important because this is what determines the radiated flux inside the bandwidth of the camera.

## **B. SPEED OF OPERATION MEASUREMENT**

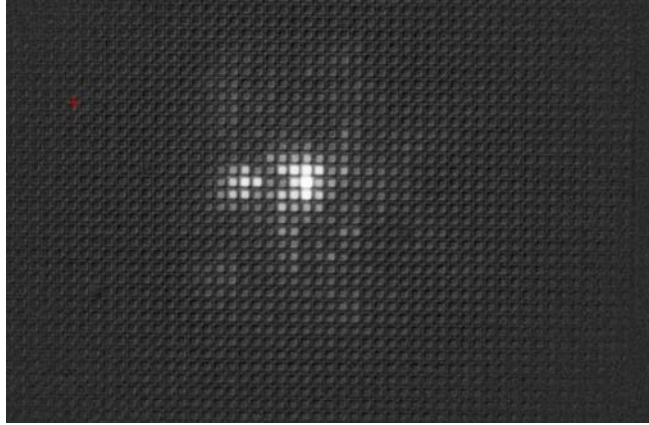
To verify the accuracy of our FE model and to determine the speed of operation of the sensor, its response was measured by pulsing the QCL. This was accomplished by gating the QCL power supply between 0.25 Hz and 30 Hz and measuring the output peak to peak temperature difference. Figure 11 shows schematics of the setup used to take the measurement. The laser used to illuminate the sensor is the 4.75 THz EasyQCL-1000 made by LongWave Photonics LLC. The laser is contained inside a vacuum chamber and cooled to below 30 K [15]. A 38 mm Parylene N lens is used to focus the THz beam onto the sensor. In order to eliminate the loss of thermal energy due to convection, the sensor was placed into a vacuum chamber. The THz side of the vacuum chamber has a 2 mm thick Tsurupica window, which transmits about 60% of the THz radiation and blocks radiation in the IR band [16]. The IR side of the vacuum chamber has a 2 mm thick zinc selenide window, which transmits about 90% of the IR radiation.



Experimental setup consisting of a 4.8 THz QCL where the THz beam is focused using a 38mm Parylene N lens onto the THz-to-IR sensor. The Sensor is inside a vacuum chamber with a Tsurupica window on the THz side and a zinc selenide window on the IR side. An IR camera was used to probe the IR side of the sensor. A laptop, running Research IR, was connected to the IR camera to record data.

Figure 11. Experimental Setup for Speed of Operation Measurements

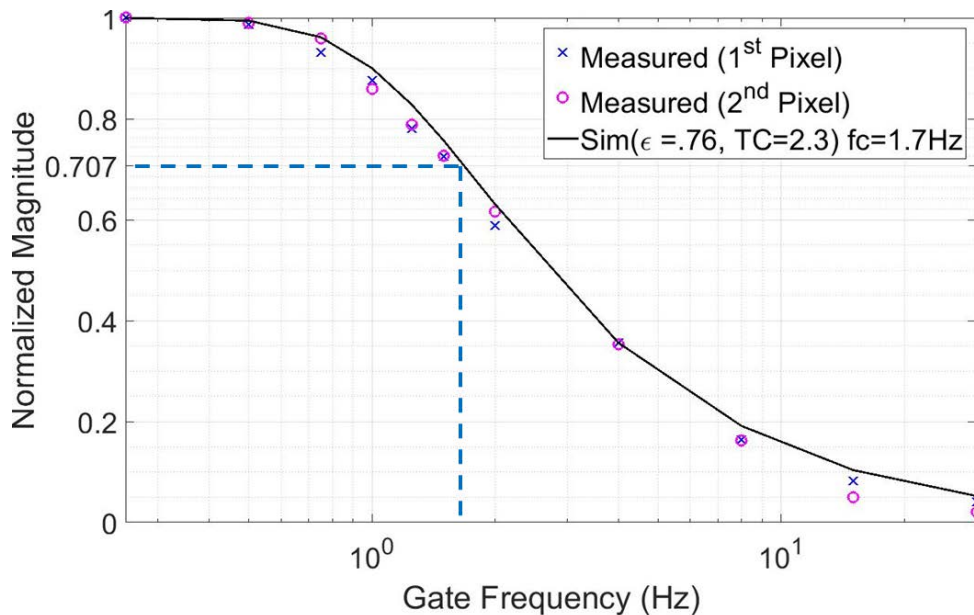
Figure 12 shows the IR image of the THz-to-IR pixels heated by the QCL beam. The region of interest used to measure the average temperature was a three pixels by three pixels area, which was fully contained a single THz pixel. In order to measure the frequency response, the QCL was gated using a waveform generator between 0.25 Hz and 30 Hz.



Screenshot, from ResearchIR, of the sensor pixels being illuminated by the QCL.

Figure 12. Screenshot from ResearchIR

The peak-to-peak temperature difference was recorded and plotted as a function of gate frequency as shown in Figure 13. This measurement was conducted on two pixels of the sensor and resulted in a cut-off frequency of 1.6 Hz. These results were used in adjusting our FE model simulation also shown in Figure 13 and outlined in section IVA.



Speed of operation measurement of two different pixels compared to simulation results. The experimental cutoff frequency was found to be 1.6 Hz, while the simulated was 1.7 Hz.

Figure 13. Speed of Operation Plot

### C. RESPONSIVITY MEASUREMENT

For the responsivity measurement, the same setup was used as for the speed of operation measurement. In order to get an estimate on the power incident onto a pixel on the sensor, a calibrated power meter was placed at the sensor's position. The QCL output power was controlled by changing the driving frequency of the QCL's LWP-PS3 power supply. Figure 14 shows the setup for measuring incident power.

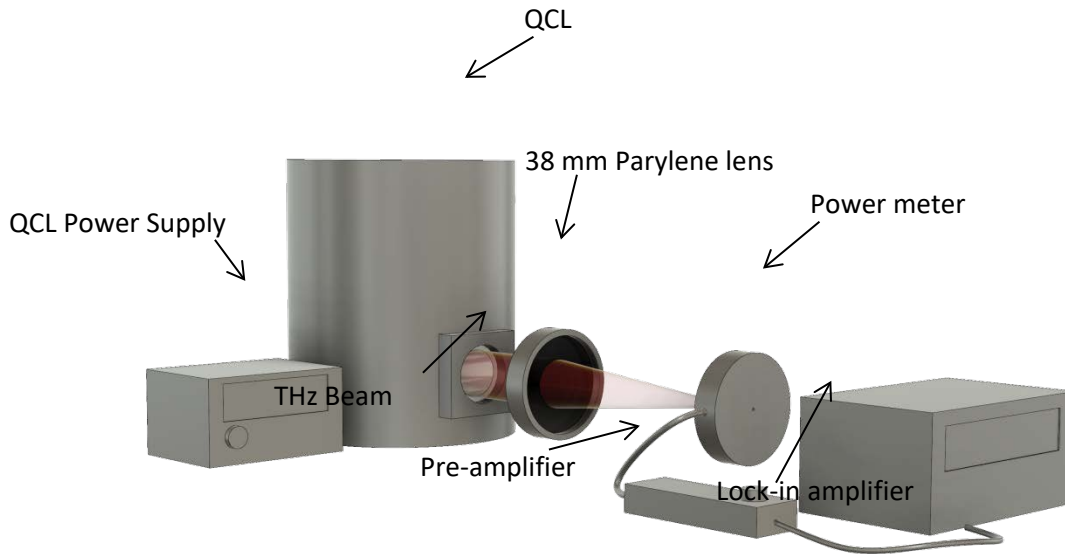
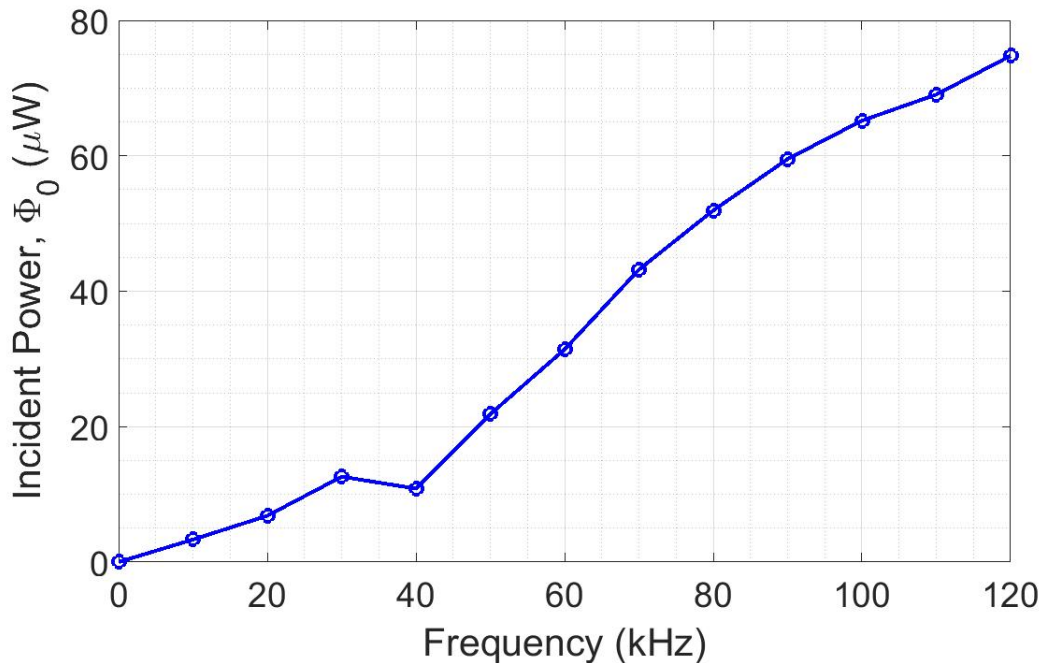


Diagram showing the setup for measuring the incident power. The 3.8 THz QCL is being controlled by a LWP-PS3 power supply. The incident THz beam is being focused by a 38mm Parylene N lens. The incident power is being detected by a THz-20 power meter and then goes through a pre-amplifier before going to the lock-in amplifier, where the output can be read.

Figure 14. Setup for Measuring Incident Power

The power supply was set to 17.20 V with a pulse width of 6300 ns, an output impedance of 1  $\Omega$  and a Duty Cycle of 79.94%. The output power was controlled by adjusting the output frequency, as shown in Figure 15. For detecting the incident power, a THz power meter was used. The power meter is a THz-20 pyroelectric meter connected to a current pre-amplifier. Both the power meter and pre-amp are manufactured by Stanz-und LaserTechnik. The setup provides a response of 58.8 V/W.

Using the setup described above the QCL power was recorded by varying the frequency of the power supply from 0.01 kHz to 120.01 kHz and the incident power at the detector,  $\Delta\Phi_0$ , was recorded. In order to estimate the incident power on one pixel of our sensor, the total power recorded was divided by the approximate number of pixels the incident beam covered, determined by using a screen shot from the IR camera, see Figure 12. Figure 15 shows the relationship between frequency of the QCL power supply and incident power on a pixel of the sensor. These results will be used in determining responsivity.

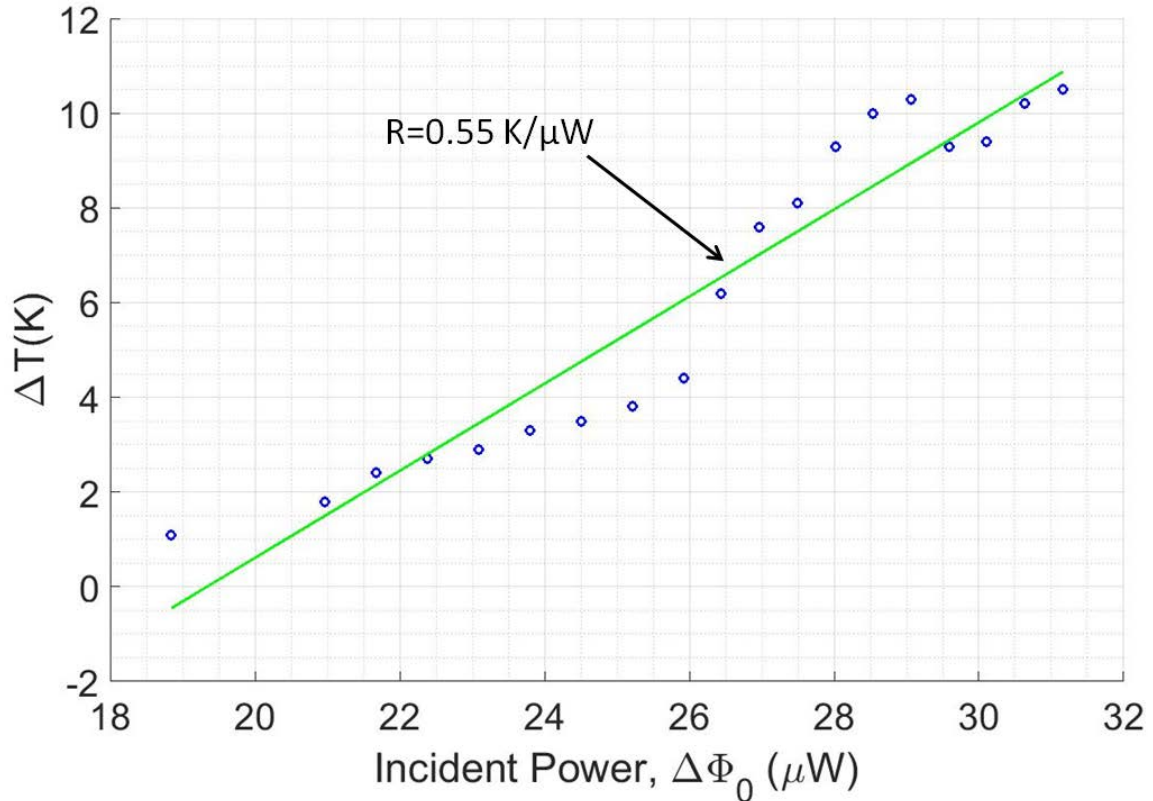


Graph showing the incident power on a pixel of the sensor as a function of the frequency of the QCL power supply.

Figure 15. Measured Incident Power,  $\Phi_0$ , as a Function of QCL Power Supply Frequency

The setup shown in Figure 11 was also used to measure responsivity. This was obtained by measuring the peak-to-peak temperature difference using the FLIR IR camera as the frequency of the QCL power supply is varied. Figure 16 shows the responsivity data. The temperature was recorded using the measurement cursor analysis

tool as previously described. The data from Figure 15 was used to determine the incident power on the pixel. The same pixel was measured for all the data points. The responsivity was measured to be approximately  $550 \text{ mK}/\mu\text{W}$ . A  $\Delta T$  could not be measured for an incident power less than  $30 \mu\text{W}$  due to distortion in the QCL beam caused by a shifting of the laser mode. This phenomenon is explained in more detail in Ashmore's thesis [11].

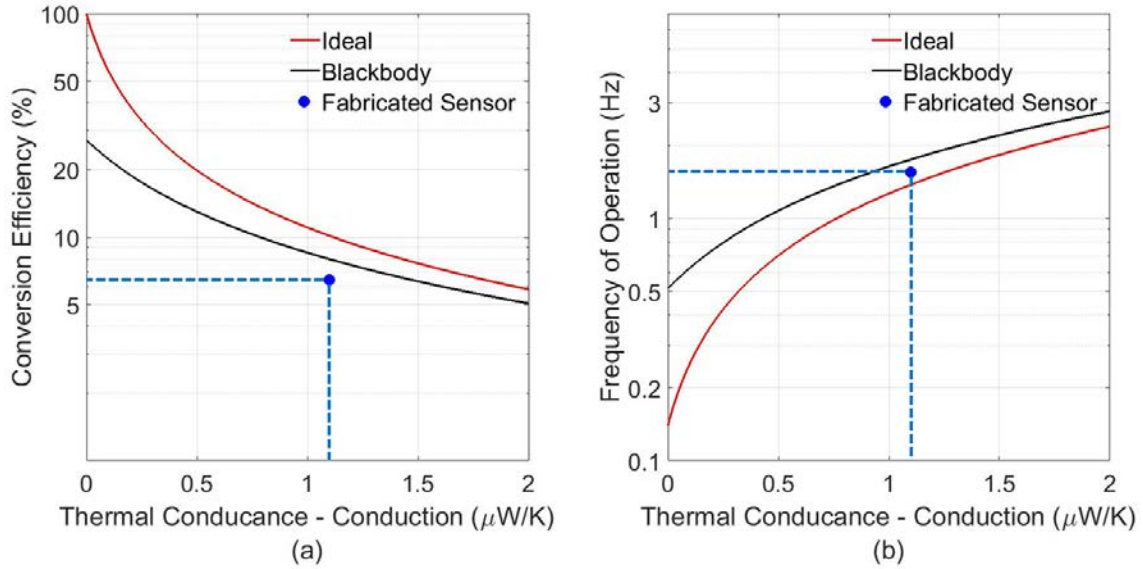


Graph showing the responsivity of the sensor. Suspected that the two regions are due to two different operating modes of the QCL.

Figure 16. Sensor Responsivity

Even though the backside of the sensor did not have an optimized metamaterial for IR emission at the frequency band of the FLIR T1030, the THz-to-IR sensor showed performance comparable with other THz detection techniques [10]. The frequency response measurement proved to be useful in finding the thermal conductivity of  $\text{SiO}_x$ , needed for the FE models. The conversion efficiency and the frequency of operation of

the measured sensor were computed and compared with the ideal and blackbody cases, previously discussed (Figure 17).



Graphs showing the conversion efficiency and frequency of operation of the fabricated sensor. Fabricated sensor uses metamaterial tuned for 4.8 THz for both sizes of the sensor. Absorption and spectral radiance of the metamaterial can be seen in Figure 8.

Figure 17. Conversion Efficiency and Frequency of Operation of the Fabricated Sensor

## IV. FINITE ELEMENT MODELING

The metamaterial and sensor structures were simulated using COMSOL Multiphysics. Two main models were used, the first being a quarter sensor simulation using the Heat Transfer in Solids and Solid Mechanics module. This model was used to analyze the heat transfer characteristics and frequency response of the sensor. The second model used the Electromagnetic Waves module to analyze absorption/emission characteristics for different metamaterial geometries in a unit cell basis. This work primarily focuses on the study of metamaterial broadband emission in the IR range and more specifically, within the range of our IR camera, 7.5–14  $\mu\text{m}$  (20–40 THz).

### A. COMSOL HEAT TRANSFER IN SOLIDS AND SOLID MECHANICS MODEL

COMSOL, along with the Heat Transfer in Solids and Solid Mechanics Modules were used to simulate the heat transfer and speed of operation characteristics of our sensor. Due to symmetry (see Figure 6) only one quarter of the sensor was simulated to reduce simulation time. Figure 18 shows the 3D model used in the simulation; note that the vertical axis is exaggerated for visual purposes. The 3D model was constructed to be a precise representation of the measured sensor (see chapter II) with both sizes having the same metamaterial tuned to 4.8 THz. The geometry of the model is the same as shown in Figure 6 and with the dimensions given in Table 1.

Table 1. Geometric Dimensions of COMSOL Thermal 3D Model

	s ( $\mu\text{m}$ )	g ( $\mu\text{m}$ )	t <sub>R</sub> (nm)	t <sub>D</sub> ( $\mu\text{m}$ )	t <sub>GP</sub> (nm)	t <sub>L</sub> ( $\mu\text{m}$ )
COMSOL Sensor	14.5	2	220	1.1	220	2.2

In the Heat Transfer in Solids module, the initial temperature was set to 293.15 K and the substrate frame was held at this fixed initial temperature, this allowed the substrate frame to act as a heat sink. The top and bottom areas of the sensor were set as

diffuse surfaces with the emissivity set to 0.76, which is the measured emissivity (see section IIA). The symmetry boundaries were set as thermal isolators. A heat flux was applied to the front side of the sensor with a value of  $25 \text{ W/m}^2$  to simulate a total power of  $1 \mu\text{W}$  absorbed by the THz metamaterial.

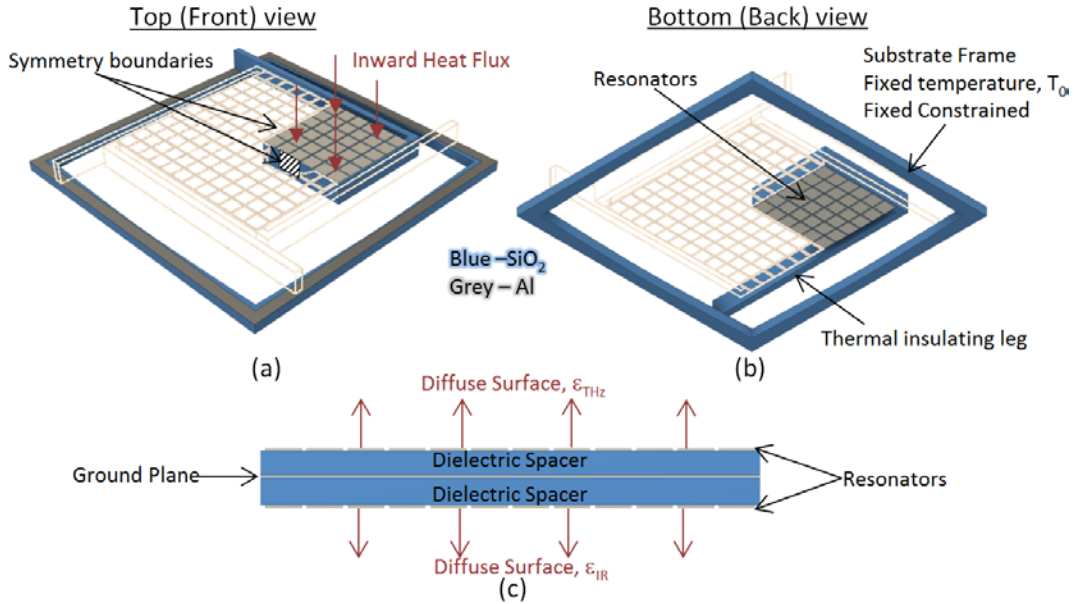


Figure showing the COMSOL thermal model. Due to symmetry of the sensor, a quarter sensor was used to decrease simulation time. The vertical dimension was exaggerated in order to see the layer easier.

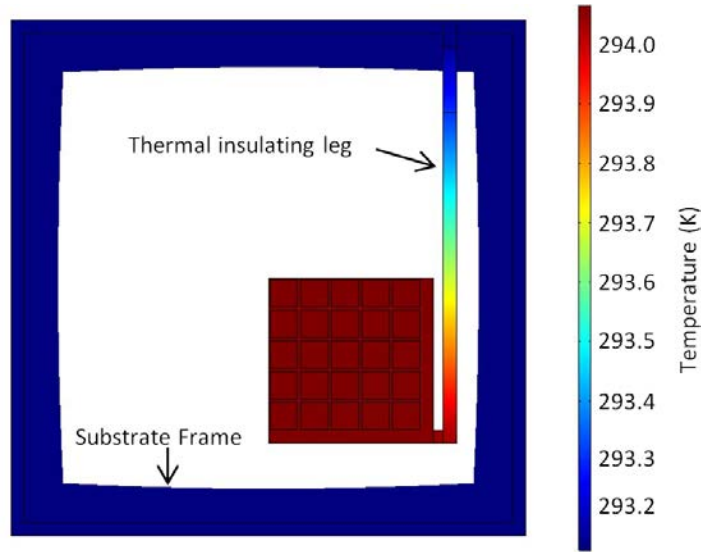
Figure 18. COMSOL Thermal Model

Meshing was conducted using a free triangular mesh placed on the top surface. A one element mesh was swept through all domains. Table 2 shows the materials used in the simulation along with their properties. These properties were determined from literature and our measurements. The structure of the sensor was fabricated using low stress silicon-rich silicon oxide ( $\text{SiO}_2$ ), which is non-stoichiometric. Most of the mechanical properties are very similar to  $\text{SiO}_2$ , however the richer concentration of silicon affects the thermal conductivity (TC) directly impacting the thermodynamics of the sensor. The TC of the  $\text{SiO}_x$  was obtained by fitting the simulated speed of operation with the measured (see Figure 13). The dielectric TC was adjusted until the thermal time constant of the simulated and measured matched.

Table 2. Material Properties Used in COMSOL Simulation

Material	Heat Capacity [J/(kg K)]	Density [kg/m <sup>3</sup> ]	Thermal conductivity [W/(m K)]	Young's modulus [Pa]	Poisson's ratio	Refractive index	Electric Conductivity [S/m]	Thermal expansion [1/K]
SiO <sub>x</sub>	703	2200	2.4	68x10 <sup>9</sup>	0.17	2.0-0.05i	---	0.5x10 <sup>-6</sup>
Al	900	2700	237	70.0x10 <sup>9</sup>	0.35	---	10x10 <sup>6</sup>	25x10 <sup>-6</sup>
Si	700	2329	130	170x10 <sup>9</sup>	0.28	---	---	2.6x10 <sup>-6</sup>

Figure 19 shows the steady state temperature distribution of the pixel from the COMSOL heat transfer simulation.

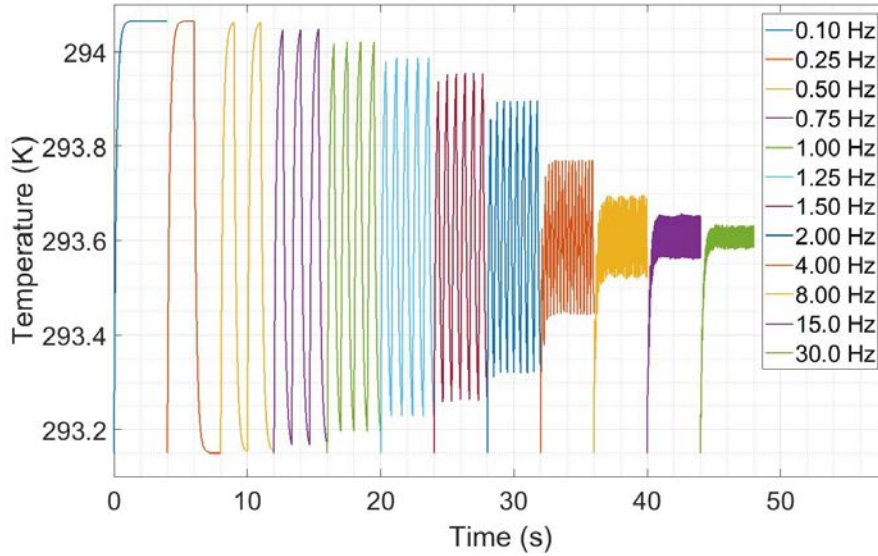


Simulated steady state temperature distribution with a absorbed power of 1 $\mu$ W.

Figure 19. Steady State Temperature Distribution

The frequency of operation of the sensor was simulated by conducting a parametric sweep of the gate frequency from 0.1 Hz to 30 Hz. Figure 20 shows the temperature of the sensor as the incident heat flux is gated. The temperature of the sensor was derived by taking the volume integral of the sensing element (central part) portion of the sensor. This data was used to determine the peak-to-peak temperature for each gate

frequency. The simulation results for SiO<sub>x</sub> thermal conductivity of 2.4 W/(mK) is plotted in Figure 13 for comparison.



Plot of temperature vs. time of the sensor as incident thermal energy is gated from 0.1 Hz to 30 Hz. Temperature was calculated in COMSOL by taking a volume integral of the temperature of the sensing element (central part) of the sensor.

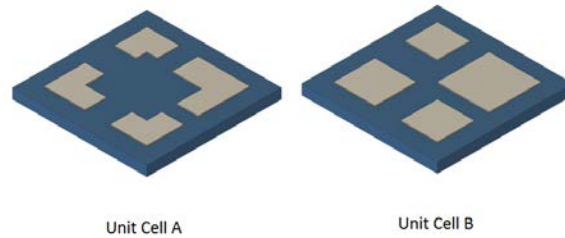
Figure 20. Temperature of the Sensor as the Incident Thermal Energy is Gated Between 0.1 Hz and 30 Hz

Since the simulated incident power is 1  $\mu\text{W}$  and the absorptivity is about 90% and the steady state, low frequency, peak-to-peak temperature in Figure 20 is about 0.9 K the simulated responsivity is approximately 800 mK/ $\mu\text{W}$ , which is close to the measured results shown in Figure 16. This model will be used in future designs where geometry and constituent materials will be selected to optimize the sensor for specific applications.

## B. COMSOL ELECTROMAGNETIC WAVES MODEL

COMSOL with Electromagnetic Wave module was used to explore different geometries for broad band IR metamaterial. The goal was to get a high emissivity within the band of the IR camera, 20–40 THz, while minimizing the emissivity outside the band of the IR camera. Figure 21 shows the different geometries explored for creating a

broadband IR emitter. Each unit cell represents a single unit of a matrix which makes up a pixel of the sensor. Unit Cell A is based off of a geometry developed by Gong et al. [17]. Unit Cell B with varying square resonator sizes was also employed in our simulations.



Different unit cell design explored in developing a broad band IR emitter. Unit Cell A was developed based on an idea presented by Gong et al. [17]. Unit Cell B builds on the idea used to develop the unit cell for the terahertz absorber.

Figure 21. Explored Unit Cell Geometries for Producing a Broad-Band Emitter

In COMSOL, the Electromagnetic Waves module with Frequency Domain was used for simulations. Figure 22 shows the 3D model used in the simulation. The metamaterial unit cell is composed of an aluminum ground plane with a thickness of  $t_{GP}$ , a  $\text{SiO}_2$  dielectric spacer with a thickness of  $t_D$  and aluminum resonators with thickness of  $t_R$ . The metamaterial unit cell is sandwiched by air layers. There are two ports defined, Port 1 and Port 2. Port 1 is an active port with a port input power of  $1 \mu\text{W}$  and Port 2 is a passive port. This configuration allows the computation of the scattering parameters  $S_{11}$ , and  $S_{21}$ , and consequently reflectivity, which is given by  $|S_{11}|^2$ , and transmissivity, given by  $|S_{21}|^2$ . Because of the aluminum ground plane, transmissivity is near zero. The absorptivity is calculated by taking a volume integral of the resistive loss within the unit cell and then normalizing it by dividing by the incident power. Perfectly matched layers, capped by scattering boundary condition, were placed on the outside of the ports. This ensured that no energy was reflected back to the port due to artificial boundaries. Floquet periodic boundary conditions were applied to all four sides of the model. An extremely fine, free triangular mesh was applied to surface to ensure mesh side was much less than

the wavelength. A two element mesh was swept through the vertical components of the resonators and the ground plane. A ten element mesh was swept through the dielectric spacer and an eight element mesh was swept through the air portions, with an element ratio of 70 and symmetric distribution. Material properties used are in Table 2.

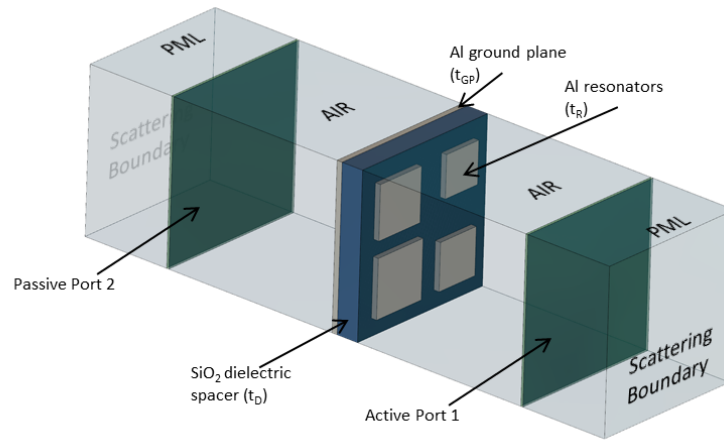


Diagram showing unit cell model used in COMOL. Metamaterial sandwiched by air and capped by Perfectly Matched Layers (PML) and scattering boundaries applied to the ends. In green is a passive and active port with a port input power of  $1 \mu\text{W}$ . A Floquet periodic boundary condition was allied to all four sides.

Figure 22. COMSOL Electromagnetic Wave Model

In order to establish a methodology for the unit cell design and understand the geometrical parameters, a constant refractive index was used over the entire frequency range for the dielectric layer. Later, frequency dependent refractive index for silicon nitride was used in order to compare the simulations with fabricated Al/SiN<sub>x</sub>/Al metamaterial films.

### 1. Unit Cell A: Sectional Asymmetric Structure [17]

The first geometry explored was based off of a paper by Gong et al. [17]. In his paper he develops a broadband terahertz perfect absorber by using a unit cell that is composed of quarter sections of ring resonators. For this set of simulation, the dimensions were scaled down and the dimensions and resonator layout is illustrated in

Figure 23. Each resonator is a square, with a side width  $S$ , with a square notch taken out of it. The notch for each resonator is formed in such a way so the resonator width,  $w$ , is constant for all resonators. All resonators are kept at a constant distance,  $b$ , from the edge of the unit cell. The width of the unit cell is represented by  $p$ . There are many ways to define the geometry for this unit cell, for example the resonator locations could have been restrained by a constant distance between each resonator or each resonator could have been centered in each quadrant but in order to simplify the model and parameters the layout illustrated in Figure 23 were used.

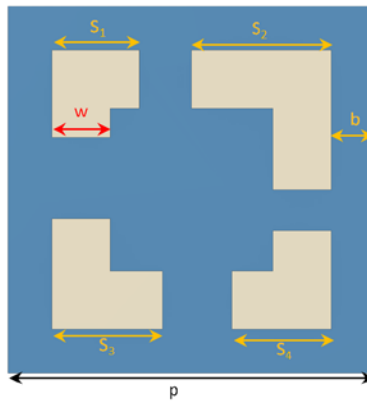


Diagram illustrating the geometries used to define unit cell A. the  $S$  values are the width of the resonators. While,  $w$  is the segment width of the resonators and applies to all the resonators.  $b$  is the margin distance between the resonators and the boarder of the unit cell.  $p$  is the width of the unit cell and is defined as  $p = 2(b + S_2)$ .

Figure 23. Unit Cell A Geometry

To get an understanding how the different parameters affected the emissivity, four simulations were carried out, each varying some parameter. The three parameters that were varied were  $w$ , the scale, and dielectric thickness. First the width of the resonator segments,  $w$ , was varied between  $0.3 \mu\text{m}$  and  $1.3 \mu\text{m}$ . The most promising resonator segment width was then used as the scale was varied. This was accomplished by applying a scaling factor to each of the resonators, keeping  $w$  constant and scaling  $p$  appropriately. For this simulation  $p$  was defined as  $p = 2(b + S_2)$  (see Figure 23). The most promising

scaling factor was then used when varying the dielectric thickness. Table 3 outlines the geometries used in each of the simulations.

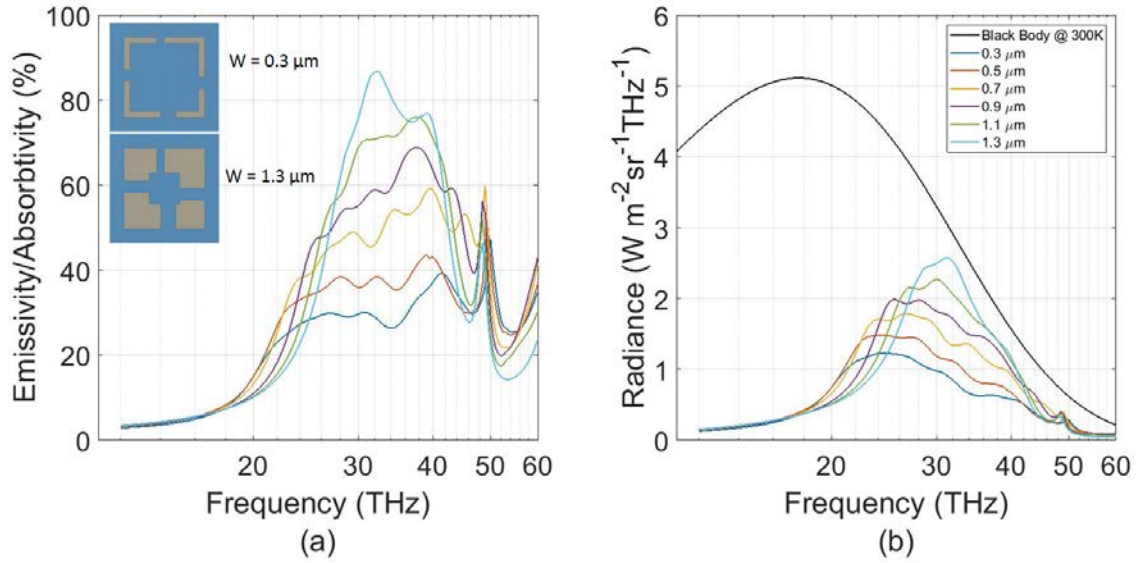
Table 3. Geometries Used in Unit Cell A Simulations

	S <sub>1</sub> [μm]	S <sub>2</sub> [μm]	S <sub>3</sub> [μm]	S <sub>4</sub> [μm]	b [μm]	p [μm]	w [μm]	t <sub>D</sub> [nm]
Vary w	1.7	2.1	1.9	1.5	0.75	5.7	0.3-1.3	350
Vary scale	sf <sup>†</sup> (1.7)	sf <sup>†</sup> (2.1)	sf <sup>†</sup> (1.9)	sf <sup>†</sup> (1.5)	0.75	Var <sup>†</sup>	1.1	350
Vary diel	1.9	2.3	2.1	1.7	0.75	6.1	1.1	350-800
Optimized	2.0	2.4	2.2	1.7	0.75	6.3	1.4	600

Table shows dimensions used for the simulation in this section. Optimized geometry was used to maximize in-band radiance. t<sub>GP</sub> and t<sub>R</sub> were kept constant at 60 nm.

<sup>†</sup> - To vary the scale, a scaling factor, sf, was applies to each of the resonators and the size of the unit cell, p, was scaled accordingly by defining it as  $p = 2(b + S_2)$ .

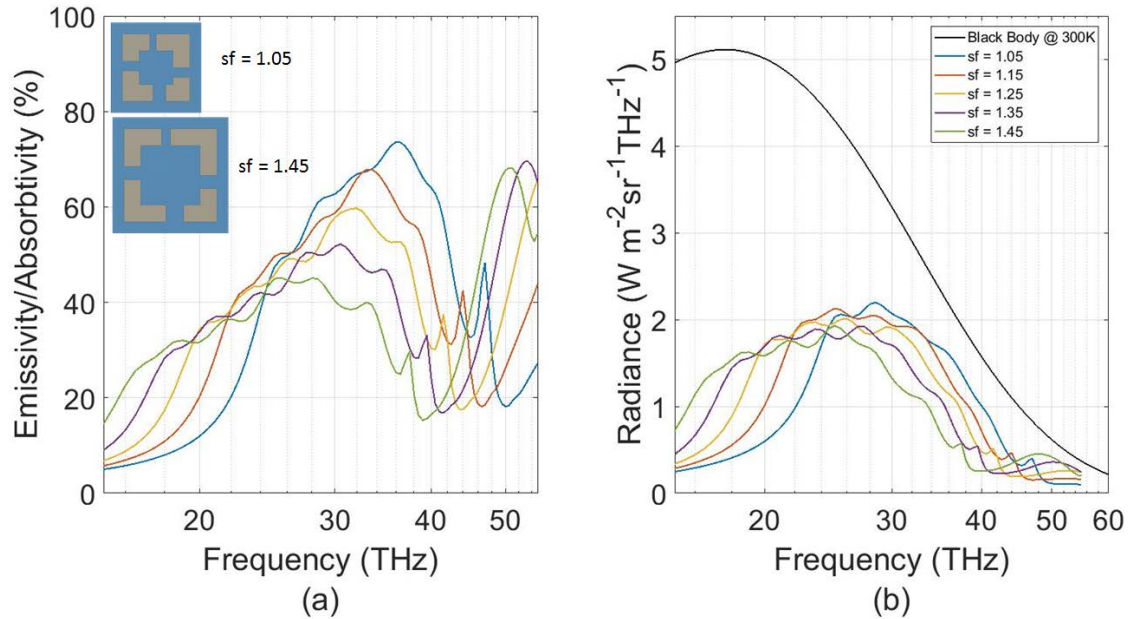
Figure 24 shows the emissivity and spectral radiance of the unit cell as the resonator segment width, w, is varied. As illustrated in the figure, as the resonator segment width decreases, the resonator area also decreases. This seems to reduce the overall emissivity of the unit cell. As w increases the emissivity band width decreases but the peak emissivity increases. This seems to show that as the surface area of the resonator is changed for a constant unit cell area, it affects the magnitude and bandwidth of the emissivity curve. This indicates that emissivity is proportional to the fill factor (surface area of the resonators divided by surface area of the unit cell). But, as the w increases the bandwidth of the emissivity curve decreases. Therefore, when choosing w, bandwidth needs to be taken into consideration. Thus, bandwidth can be controlled with either adjusting the square sizes or adjusting w and the magnitude of the emissivity curve can be controlled using dielectric thickness or adjusting w. These parameters will need to be balanced and taken into consideration when defining a geometry to get a certain emissivity curve.



Plots comparing emissivity and spectral radiance as resonator segment width,  $w$ , are varied between  $0.3 \mu\text{m}$  and  $1.3 \mu\text{m}$ , see Table 3 for dimensions. (a) shows the emissivity along with to-scale diagrams of the unit cell with  $w = 0.3 \mu\text{m}$  and  $w = 1.3 \mu\text{m}$ . (b) shows the spectral radiance as  $w$  is varied along with spectral radiance of a black body at 300 K as a reference.

Figure 24. Emissivity and Spectral Radiance of Unit Cell A as Resonator Segment Width is Varied

Figure 25 shows the emissivity and spectral radiance for the unit cell as resonators are scaled, see Table 3 for dimensions used. Scaling was done by applying a scaling factor to the resonators. Note that the scaling factor does not apply to  $b$  or to the resonator segment width, which are maintained at  $0.75 \mu\text{m}$  and  $1.1 \mu\text{m}$ , respectively.



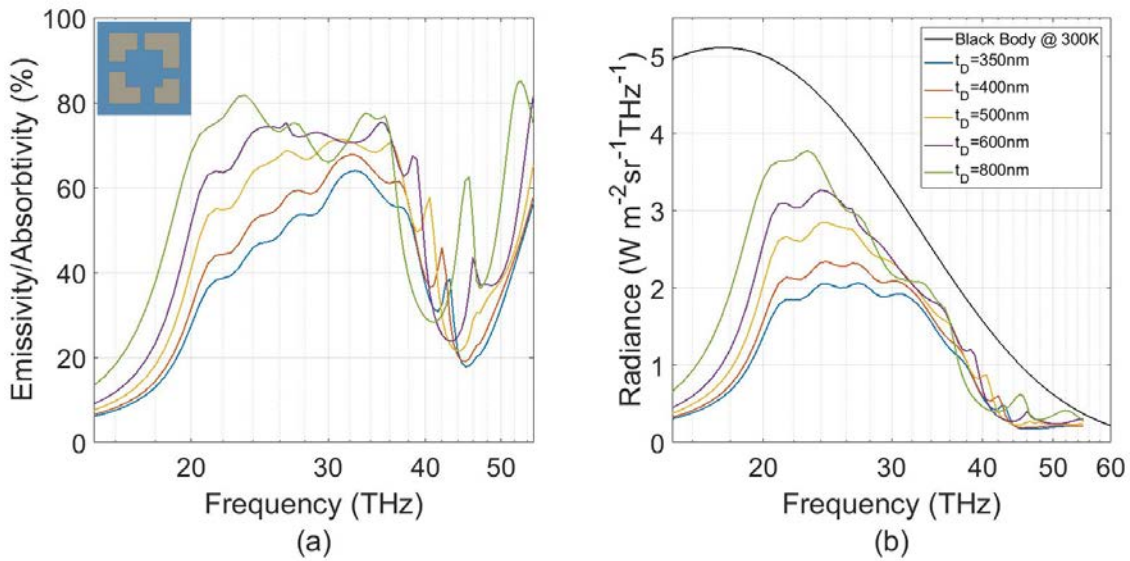
Plots comparing emissivity and spectral radiance as the resonators are scaled by a scaling factor,  $sf$ , between 1.05 and 1.45, see Table 3 for dimensions. (a) shows the emissivity along with to-scale diagrams of the unit cell with  $sf = 1.05$  and 1.45. (b) shows the spectral radiance as the scaling factor varies along with spectral radiance of a black body at 300 K as a reference.

Figure 25. Emissivity and Spectral Radiance of Unit Cell A as the Resonators are Scaled

Figure 25 shows that as the scaling of the resonators increase, the emissivity plot shifts to the left. This is to be expected because the resonant frequency of the metamaterial is inversely proportional to the resonator size. It is also interesting to note that as the resonators are scaled the resonator segment width is getting proportionally smaller. This can be seen in the diagram in the top left corner of Figure 25(a). This results in the same trend we saw in Figure 24, as  $w$  gets proportionally small there is an increase in emissivity bandwidth and a decrease in peak emissivity. The next step is to attempt to increase peak emissivity. As shown in chapter IIA, peak emissivity can be increased by increasing dielectric thickness. Therefore, it is important to know how the spectral shape of the emissivity will change as the dielectric thickness is varied.

Figure 26 confirms that as dielectric thickness is increased emissivity increases also. It is interesting to note that as the dielectric thickness increase, the emissivity does not increase proportionally across the frequency band. In general, emissivity increased

more at lower frequencies. It is also important to note that the emissivity increase drops off rapidly above 600 nm. As shown in Figure 26, the increase from 600 nm to 800 nm in dielectric thickness does not result in a significant increase in emissivity. Increasing the dielectric thickness also has the consequence of decreasing the speed of operation of the sensor. Looking at equation (4) and (10), increasing the dielectric thickness will increase the heat capacity of the sensor and therefore decrease its frequency of operation. In order to optimize the frequency of operation of the sensor, the dielectric thickness will have to be minimized. Therefore, increasing dielectric thickness in order to increase emissivity and conversion efficiency needs to be done deliberately with the understanding that there will be a loss in the speed of operation of the sensor.



Plots comparing emissivity and spectral radiance as the dielectric thickness,  $t_D$ , is scaled between 350 nm and 800 nm, see Table 3 for dimensions. (a) shows the emissivity along with a to-scale diagram of the unit cell. (b) shows the spectral radiance as the dielectric thickness varies along with spectral radiance of a black body at 300 K as a reference.

Figure 26. Emissivity and Spectral Radiance of Unit Cell A as the Dielectric Thickness is Varied

The optimized geometry in Table 3 uses the data from the results of the simulations outlined in Figures 24, 25 and 26 to develop a geometry that attempts to maximize the in-band radiance and minimize the out-of-band radiance. Figure 27 (a) and

(b) is a plot showing the emissivity and spectral radiance of the optimized geometry, respectively. The shaded area represents the in-band radiance of the IR camera,  $46.6 \text{ W}/(\text{sr m}^2)$ . The total radiance of the simulated sensor with the optimized geometry is  $54.0 \text{ W}/(\text{sr m}^2)$ . The total radiance is determined by taking the integral of the spectral radiance over the whole frequency range (only part of the frequency range shown in Figure 27(b) for illustration purposes).

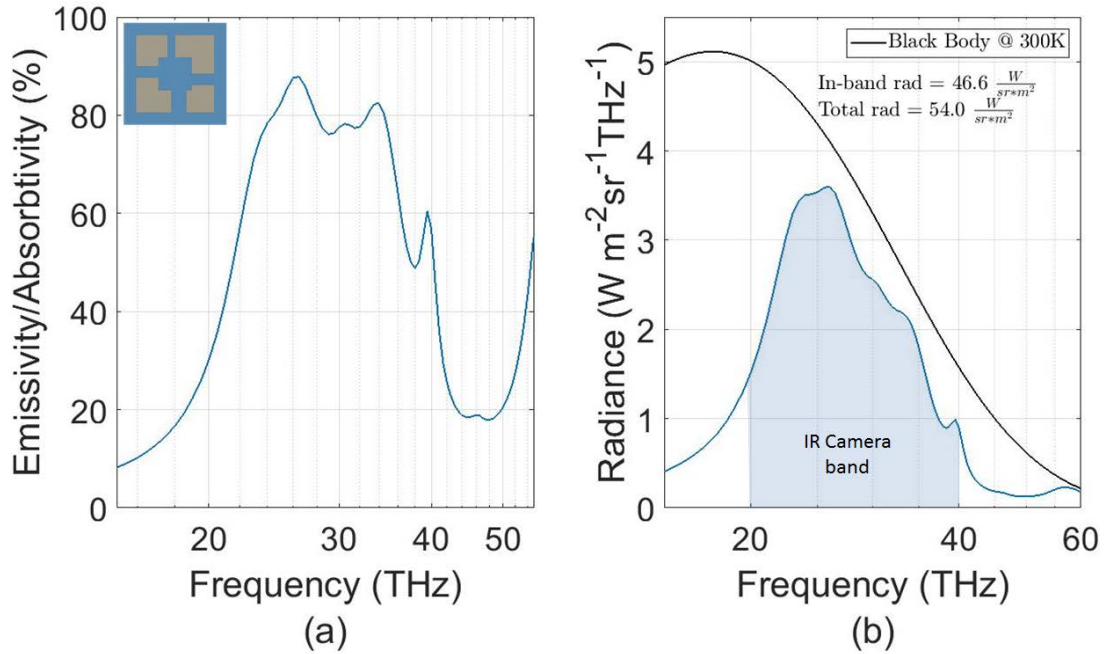


Figure shows (a) the emissivity/absorptivity and (b) the spectral radiance for the optimized unit cell A geometry. The spectral radiance was integrated over the frequency band of the IR camera and over the whole frequency band to get the in-band radiance and total radiance respectively.

Figure 27. Emissivity and Spectral Radiance for an Optimized Geometry for Unit Cell A.

In order to access the performance improvement obtained by using this configuration, the conversion efficiency and frequency of operation was estimated using equations (10) and (12). The emissivity from Figure 27(a) was used for  $\epsilon_{\text{IR}}$  and the emissivity from Figure 8(a) was used for  $\epsilon_{\text{THz}}$ . The initial temperature,  $T_0$ , was assumed to be 300 K with a  $\Delta T$  of 1 K. For calculating the thermal flux through the thermal

insulating legs, thermal conduction,  $\kappa_{th}$ , was assumed to be 4 W/(m K), a dielectric thickness for the IR side,  $d_{IR}$ , was 0.6  $\mu\text{m}$  and therefore the thermal isolating leg,  $t_L$ , was 1.7  $\mu\text{m}$  ( $d_{IR}$  plus the dielectric thickness of the THz side, 1.1  $\mu\text{m}$ ) giving a cross-sectional area of 13.6  $\text{pm}^2$  ( $t_L$  times 8  $\mu\text{m}$ ), see Figure 6. For calculating the thermal capacity a specific heat of 703 [J/(gK)] and 900 [J/(gK)] were used for  $\text{SiO}_2$  and Al, respectively. A density of 2200 [ $\text{kg}/\text{m}^3$ ] and 2700 [ $\text{kg}/\text{m}^3$ ] were used for  $\text{SiO}_2$  and Al, respectively. The surface area of the element,  $A_0$ , of 40  $\text{nm}^2$  was used. Using these parameters resulted in a conversion efficiency and Frequency of operation given in Figure 28.

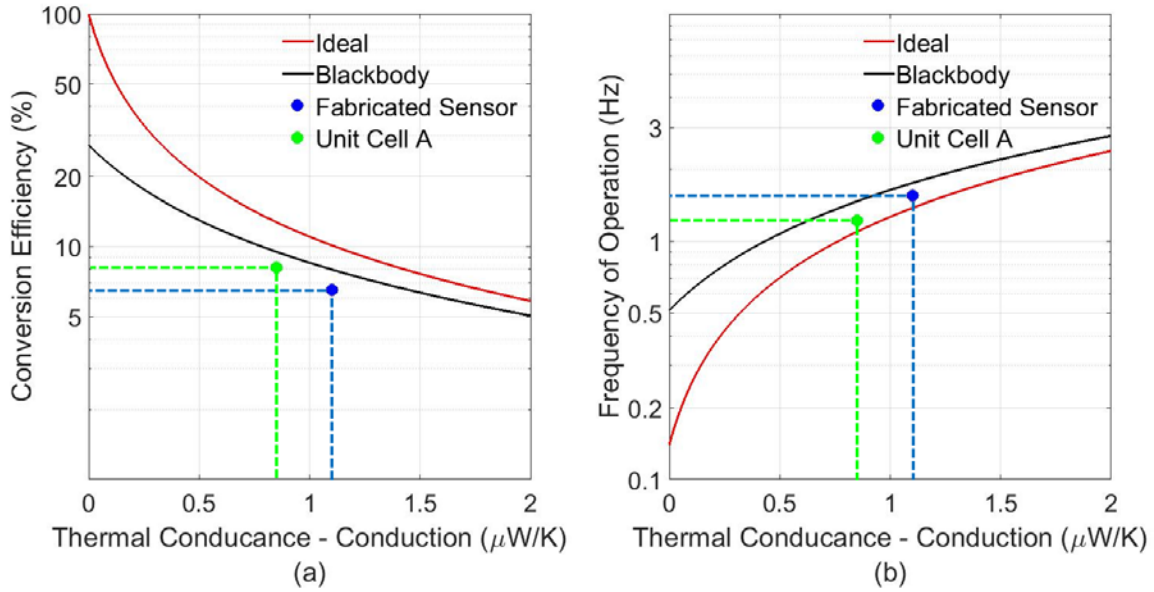


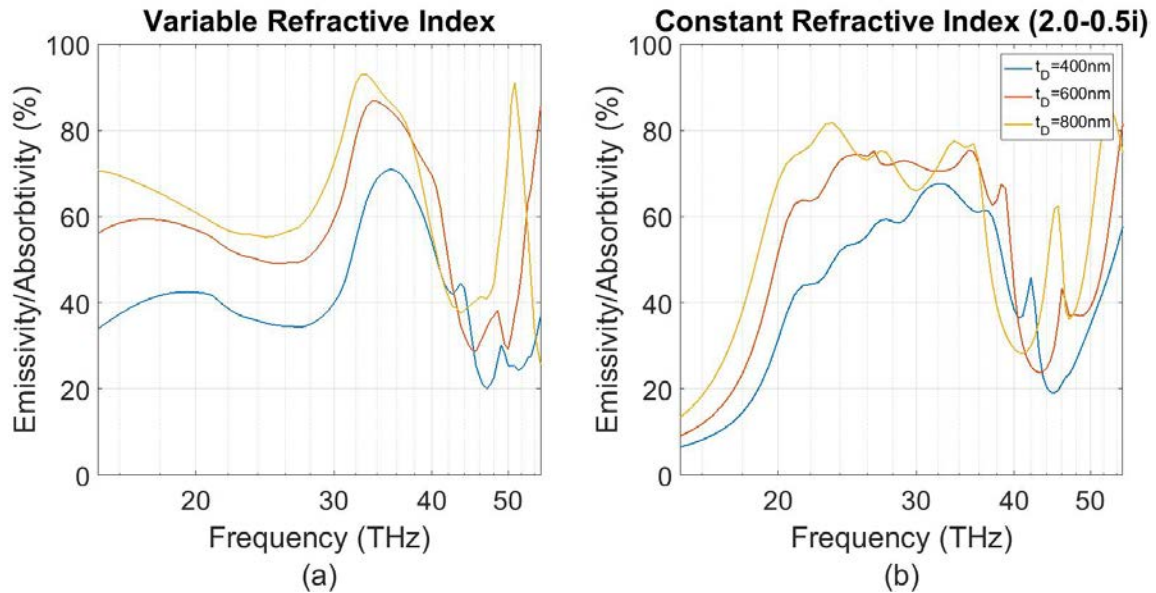
Figure showing (a) the expected conversion efficiency and (b) the expected frequency of operation of Unit Cell A. As a comparison, the conversion efficiency and frequency of operation was also plotted for the fabricated sensor.

Figure 28. Conversion Efficiency and Frequency of Operation for Unit Cell A

As shown in Figure 28, the thermal conductance of a sensor using the optimized unit cell A is lower than the thermal conductance of the fabricated sensor. This is due to the thinner dielectric layer in unit cell A, resulting in less thermal conduction through the thermal isolating legs. This is a contributing factor leading to a lower frequency of operation compared to the fabricated sensor. The higher conversion efficiency for unit

cell A can be contributed to two things. First, the ratio of in-band radiance to total radiance is higher for unit cell A. And second, the lower thermal conductance. These two factors resulted in less thermal loss in the unit cell A compared to the fabricated sensor.

In order to assess what the actual emissivity curve will look like the simulation referenced in Figure 26 was rerun using a frequency dependent refractive index for silicon nitride obtain from literature [18]. Figure 29 shows the emissivity/absorptivity as dielectric thickness is varied for the frequency dependent refractive index and for a constant refractive index. Figure 29 (a) shows some similarities to Figure 29 (b) and the differences indicate how the refractive change with frequency will affect the emissivity response. It is expected that the actual measured emissivity/absorptivity response will lie somewhere between the two plots. Once a metamaterial fil is fabricated and emissivity/absorptivity is measured the model can be refined with a more accurate refractive index.



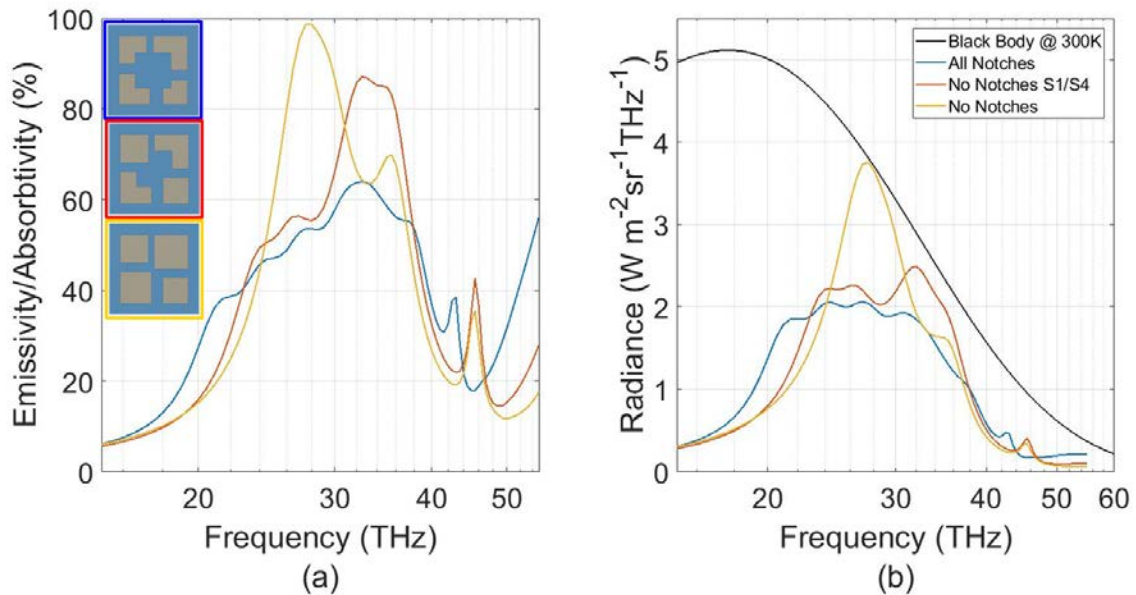
Plots showing the emissivity for different dielectric thicknesses using (a) a frequency dependent refractive index and (b) a constant refractive index. The frequency dependent refractive index is for silicon nitride and the values were taken from the website [refractivindex.info](http://refractivindex.info) [18\$].

Figure 29. Emissivity as Dielectric Thickness is Varied for Unit Cell A for a Frequency Dependent Refractive Index and a Constant Refractive Index

As shown in Figure 24 and 25, emissivity can be increased by increasing  $w$ . In order to try to maximize the emissivity, a unit cell was designed by eliminating  $w$  and using square resonators. The next section will first explore the effects of removing the notch out of the squares by eliminating the  $w$  parameter. After that, a new unit cell, unit cell B, will be evaluated that will compose of square resonators.

## 2. Unit Cell B: Square Resonators

In order to increase the overall emissivity of the metamaterial, the notches will be removed from the resonators of unit cell A, converting the brackets into squares. Figure 30 shows a comparison between three different configurations where the overall emissivity increases as the number of complete squares increases in the cell, however, the band width decreases. This can be compensated for by scaling the sensor to shift the emissivity curve to the right. The frequency bandwidth can also be adjusted by adjusting the square size of the resonators.



Plots showing the (a) emissivity and (b) spectral radiance as notches are removed from unit cell A.

Figure 30. Emissivity and Spectral Radiance of Unit Cell A as Notches are Removed

Three different parameters will be explored for unit cell B. The size of the resonators  $S_1$  and  $S_3$  will be varied in order to see how the emissivity curve changes as resonator size is changed. The dielectric thickness will also be varied. Figure 31 shows how the geometry is defined. The  $S$  values are the width of the resonators and  $b$  is the margin distance between the resonators and the boarder of the unit cell and  $p$  is the width of the unit cell. Table 4 show all the dimensions used for each of the simulations in this section.

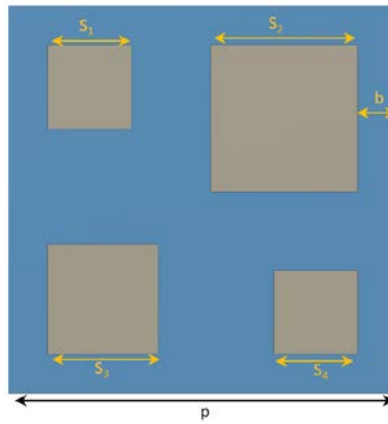


Diagram illustrating the geometry used to define unit cell B. the  $S$  values are the width of the resonators.  $b$  is the margin distance between the resonators and the boarder of the unit cell.  $p$  is the width of the unit cell and defined as  $p = 2b + S_1 + S_2 + 1.5 \mu m$ .

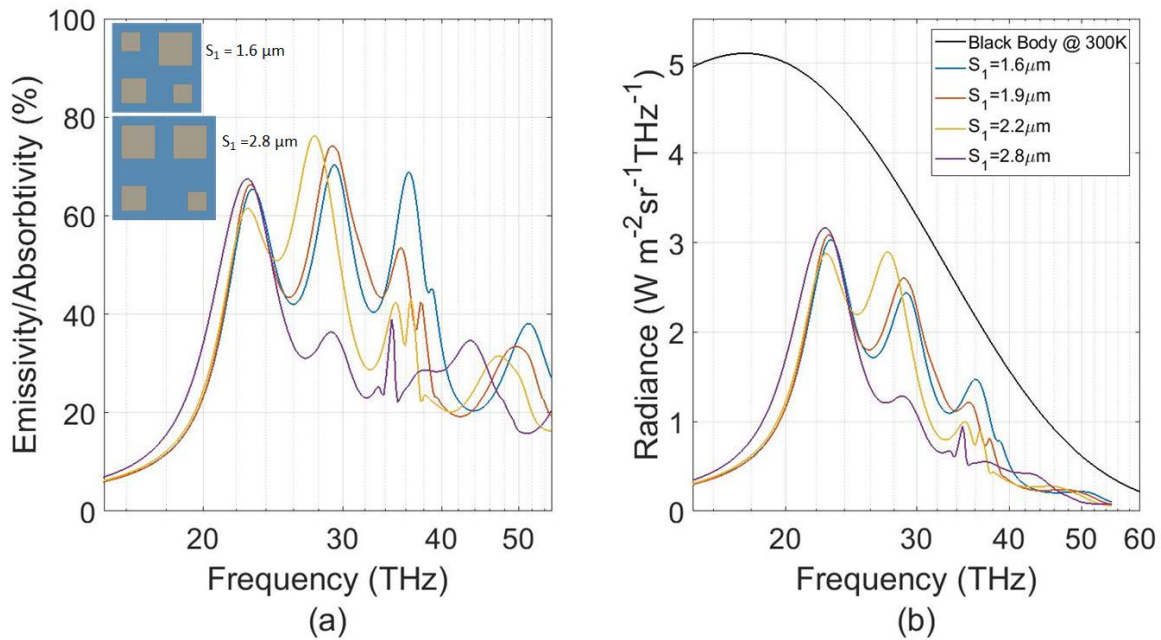
Figure 31. Unit Cell B Geometry

Table 4. Geometries Used in Unit Cell B Simulations

	$S_1$ [ $\mu m$ ]	$S_2$ [ $\mu m$ ]	$S_3$ [ $\mu m$ ]	$S_4$ [ $\mu m$ ]	$b$ [ $\mu m$ ]	$p$ [ $\mu m$ ]	$t_D$ [nm]
Vary $S_1$	1.6-2.8	2.8	2.1	1.6	0.75	7.4-8.6	350
Vary $S_3$	1.6	2.8	1.7-2.5	1.6	0.75	7.0-7.8	350
Vary diel	1.6	2.8	2.1	1.6	0.75	7.4	350-800
Optimized	1.6	2.8	2.1	1.6	0.75	7.4	600

Table shows dimensions used for the simulation in this section. The optimized geometry was used to maximize in-band radiance.  $t_{GP}$  and  $t_R$  were kept constant at 60 nm.  $p$  is size of the unit cell and defined as  $p = 2b + S_1 + S_2 + 1.5 \mu m$ .

First resonator  $S_1$  size is varied from  $1.6 \mu\text{m}$  to  $2.8 \mu\text{m}$ . It is expected that as the resonator size varies the peak frequency associated with that resonator will shift accordingly. As Figure 32 shows, as  $S_1$  increases in size the right peak gets smaller, this is expected since  $S_1$  and  $S_4$  are what contributes to those peaks. There are two interesting effects to note in Figure 32(a). First, is the drastic change in the center peak when  $S_1$  reaches  $2.8 \mu\text{m}$ . The center peak is significantly smaller. As  $S_1$  grows in size, so does the overall unit cell size and therefore resonators  $S_3$  and  $S_4$  make up a smaller percentage of the surface area which can explain the differences in the peak size of the center and right peak as  $S_1$  gets larger. Second, the right trough was not eliminated by varying the size of  $S_1$ .

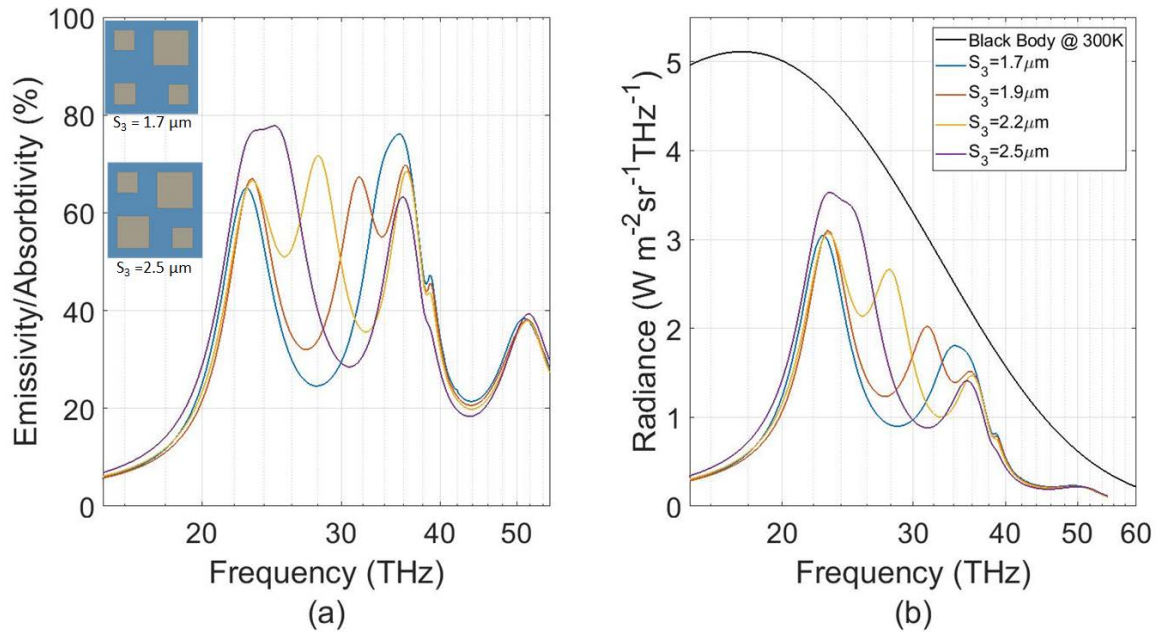


A Plot showing (a) the emissivity and (b) the spectral radiance of unit cell B as the size of  $S_1$  is varied.

Figure 32. and Spectral Radiance of Unit Cell B as the as the Size of  $S_1$  is Varied

In order to assess how the emissivity changes as the resonator square sizes change without effecting the size of the unit cell, a simulation was run varying the size of resonator  $S_3$ . As shown in Figure 33, as the size of  $S_3$  is varied from  $1.7 \mu\text{m}$  to  $2.5 \mu\text{m}$ ,

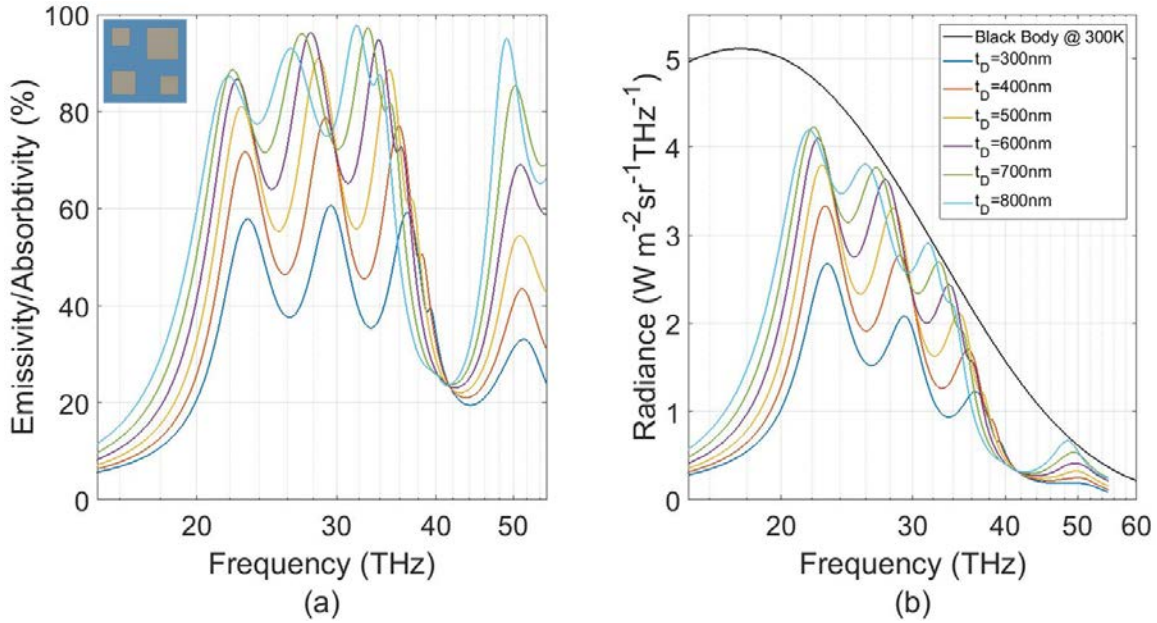
the peak smoothly shift from a higher to a lower frequency. Also, as  $S_3$  increases in size and the peak shifts away from the higher frequency peak, the higher frequency peak decreases slightly in magnitude. These effects are slightly different then when  $S_1$  was varied.



A Plot showing (a) the emissivity and (b) the spectral radiance of unit cell B as the size of  $S_3$  is varied.

Figure 33. Emissivity and Spectral Radiance of Unit Cell B as the as the Size of  $S_3$  is Varied

The main purpose of changing a resonator size would be to adjust where the emissivity peaks, however from Figure 32 and 33 one can identify the effects of fill factor and coupling between squares. Optimizing the emissivity for the desired band is not a trivial task. Figure 34 shows that peaks in the emissivity curve can be increased to close to 100% by increasing dielectric thickness. This is true until around 600 nm. At about 800 nm the emissivity peaks start to decrease.



A Plot showing (a) the emissivity and (b) the spectral radiance of unit cell B as the size of  $S_3$  is varied.

Figure 34. Emissivity and Spectral Radiance of Unit Cell B as Dielectric Thickness is Varied

Table 4 shows the geometric parameters used to obtain the response shown in Figure 35. They were chosen in an attempt to maximize in-band radiance and minimize out-of-band radiance. In Figure 35 the shaded region representing the radiance within the bandwidth of the camera. In order to maximize the emissivity the space between the resonators were minimized. But, due to fabrication limitations, the minimum distance between the resonators is limited to  $1.5 \mu\text{m}$ . The dielectric thickness of  $575 \text{ nm}$  was used and  $S_1$  was offset slightly. Using this geometry the simulation showed an in-band radiance of  $48.9 \text{ W}/(\text{sr m}^2)$  and a total radiance of  $60.0 \text{ W}/(\text{sr m}^2)$  resulting in 81.5% of the radiated energy being in-band.

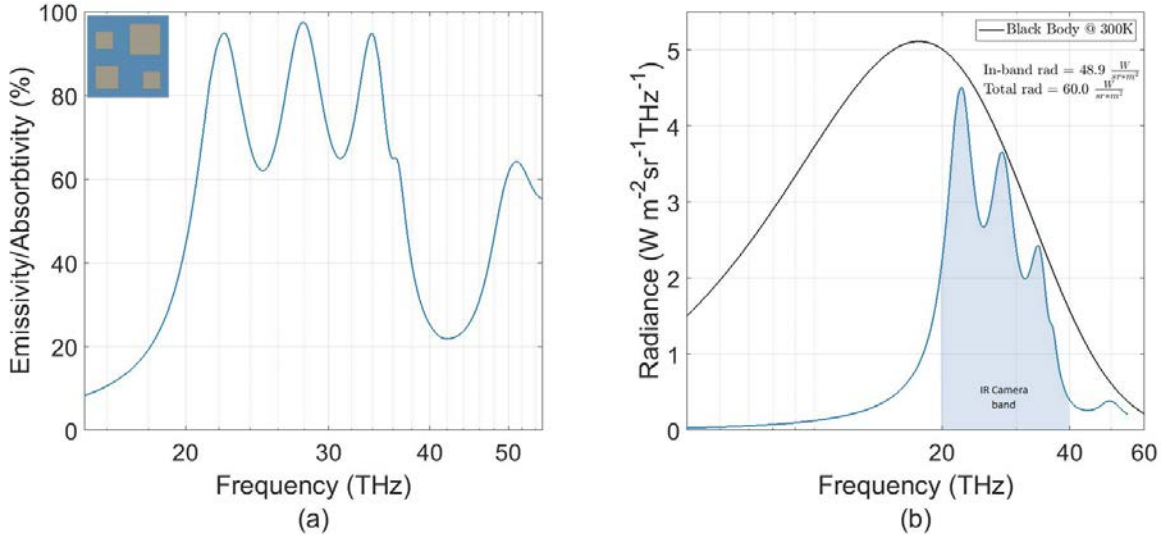


Figure shows (a) the emissivity/absorptivity and (b) the spectral radiance for the optimized unit cell B geometry. The radiance was integrated over the frequency band of the IR camera and over the whole frequency band to get the in-band radiance and total radiance respectively.

Figure 35. Emissivity and Spectral Radiance for an Optimized Geometry for Unit Cell B

Figure 36 shows the estimated conversion efficiency and speed of operation of the optimized sensor compared with the efficiency of the fabricated sensor. Conversion efficiency and frequency of operation were calculated using the same method for unit cell A except the emissivity from Figure 35(a) was used for  $\epsilon_{IR}$ . Due to a thinner dielectric layer the thermal conductance of the thermal isolating legs is lower, increasing responsivity. The conversion efficiency is also higher compared to the fabricated sensor due to a lower thermal conductance and also the emissivity being more ideal (larger in-band radiance and lower out-of-band radiance). The simulation also showed that even though the thermal conductance is lower, the speed of operation is about the same as the fabricated sensor. This is due to the thinner dielectric layer resulting in a lower heat capacitance in the sensor. The conversion efficiency and thermal conductance for unit cell B and A (Figure 28) are about the same. Even though unit cell A has a lower radiance, the ratio of in-band radiance to total radiance is about the same for both. Examining equations (2) and (10), frequency of operation is directly proportional to

radiance and therefore the higher radiance of unit cell B contributes to its higher speed of operation.

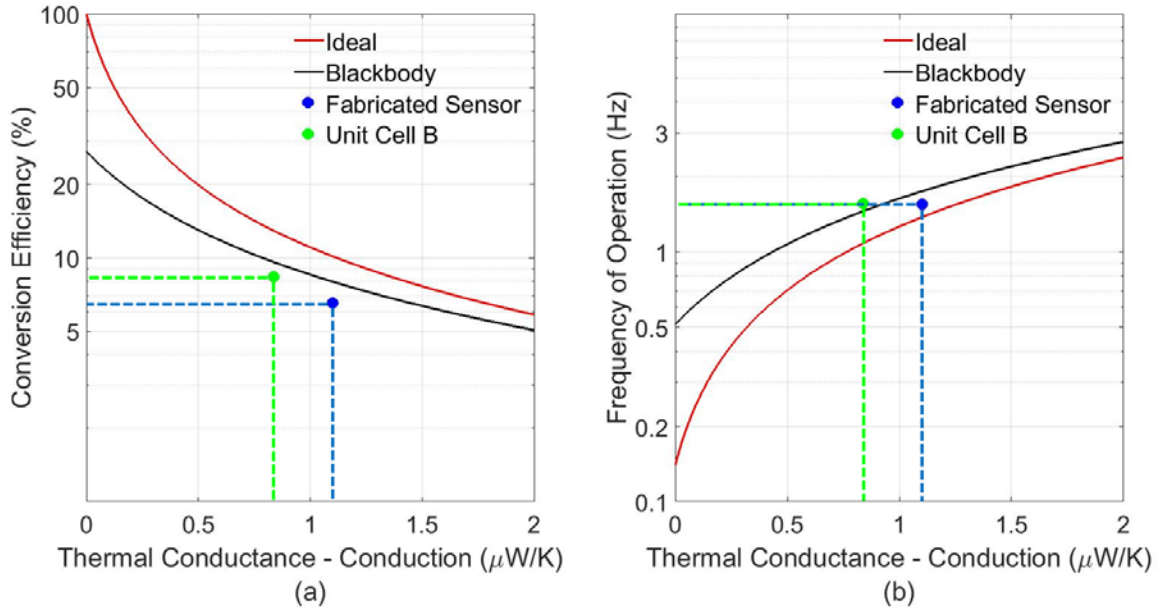


Figure showing (a) the expected conversion efficiency and (b) the expected speed of operation of Unit Cell B. As a comparison, the conversion efficiency and speed of operation was also plotted for the fabricated sensor.

Figure 36. Conversion Efficiency and speed of Operation for Unit Cell B

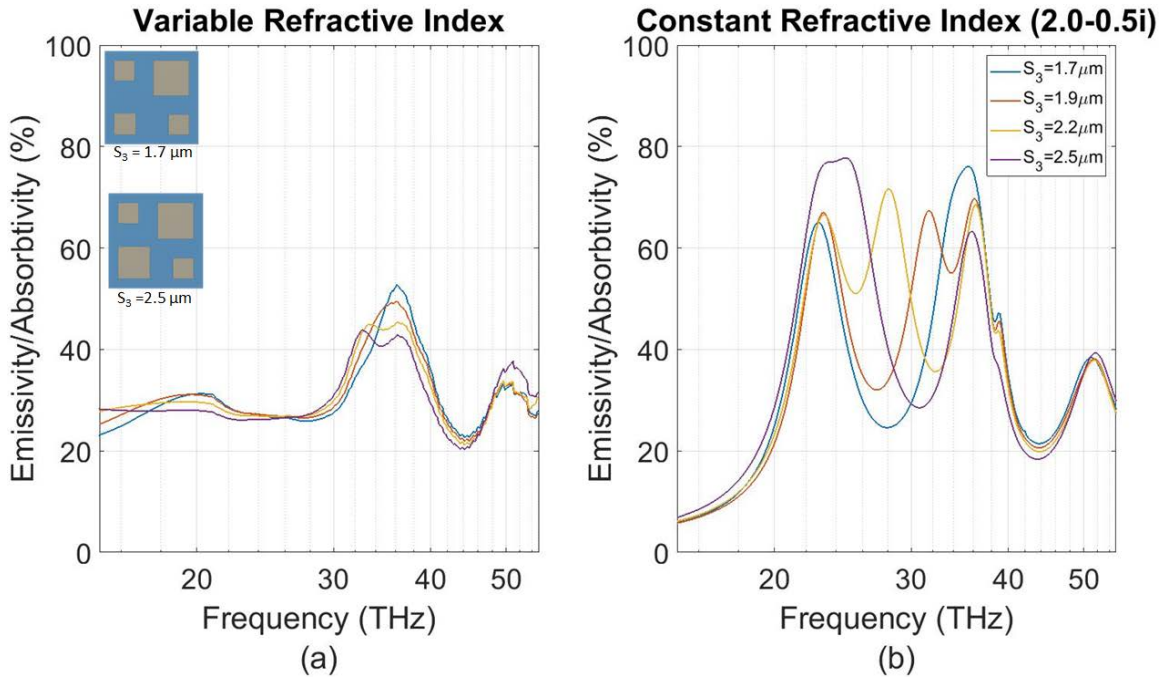
These results illustrate the importance of dielectric thickness and spectral radiance. Using these results the following properties can be generalized:

1. Conversion efficiency increases as the ratio of in-band radiance to total radiance increases (as long as thermal conductance is comparatively low).
2. Decreasing thermal conductance increases conversion efficiency.
3. Speed of operation increases as total radiance increases.
4. Speed of operation increases as thermal capacity decreases (equation (10))
5. Generally, increasing dielectric thickness will increase total radiance.

### 3. Increasing Dielectric Thickness Increases Thermal Capacitance

As shown by property 1, it is not necessary to maximize emissivity to in order to achieve high conversion efficiency. As long as the thermal losses due to conductance are not too large, high conversion efficiency can be achieved by focusing on the ratio of in-band radiance to total radiance. Looking at properties 3, 4, 5, and 6, increasing dielectric thickness can have conflicting results on frequency of operation. The overall impact of dielectric thickness on frequency of operation depends on how much total radiance and thermal capacitance are affected by the change in dielectric thickness. Therefore, increasing dielectric thickness should be done carefully as to not cancel any desired benefits.

Figure 37(a) shows the emissivity as  $S_3$  is varied using a frequency dependent refractive index for the dielectric, assumed to be silicon nitride [18]. For comparison, the emissivity shown in Figure 33 is plotted in Figure 37(b). Comparing the two emissivity plots, it would seem that varying  $S_3$  using a silicon nitride dielectric would results in a smaller frequency shift. Figure 37(a) also shows a significantly smaller emissivity compared to Figure 37(b). These results could give us a better idea on what the actual emissivity will look like when using silicon nitrite as a metamaterial spacer.



Plots showing the emissivity for different dielectric thicknesses using (a) a frequency dependent refractive index and (b) a constant refractive index. The frequency dependent refractive index is for silicon nitride and the values were taken from the website refractivindex.info [18].

Figure 37. Emissivity as the Size of  $S_3$  is Varied for Unit Cell B for a Frequency Dependent Refractive Index and a Constant Refractive Index

Unit cell B was fabricated by the SRL team at the cleanroom at NPS. The fabricated metamaterial is comprised of a 90 nm Al ground plane, a 1.1  $\mu\text{m}$  thick silicon nitride space and a 90 nm thick Al resonators. The emissivity of the sensor was measured using an FTIR. Figure 38 shows the emissivity and spectral radiance of the measured metamaterial sensor compared to the simulation. The FE simulation was run using the refractive index of silicon nitride taken from literature [18]. Figure 38 shows that the shape of the simulated emissivity closely matches that of the experimental. The discrepancies are expected as the silicon nitride data is not from the films fabricated at NPS. Using this data, the FE model can be fitted to the experimental results and the NPS silicon nitride optical properties can be obtained. This will refine the model allowing more accuracy on the sensor design.

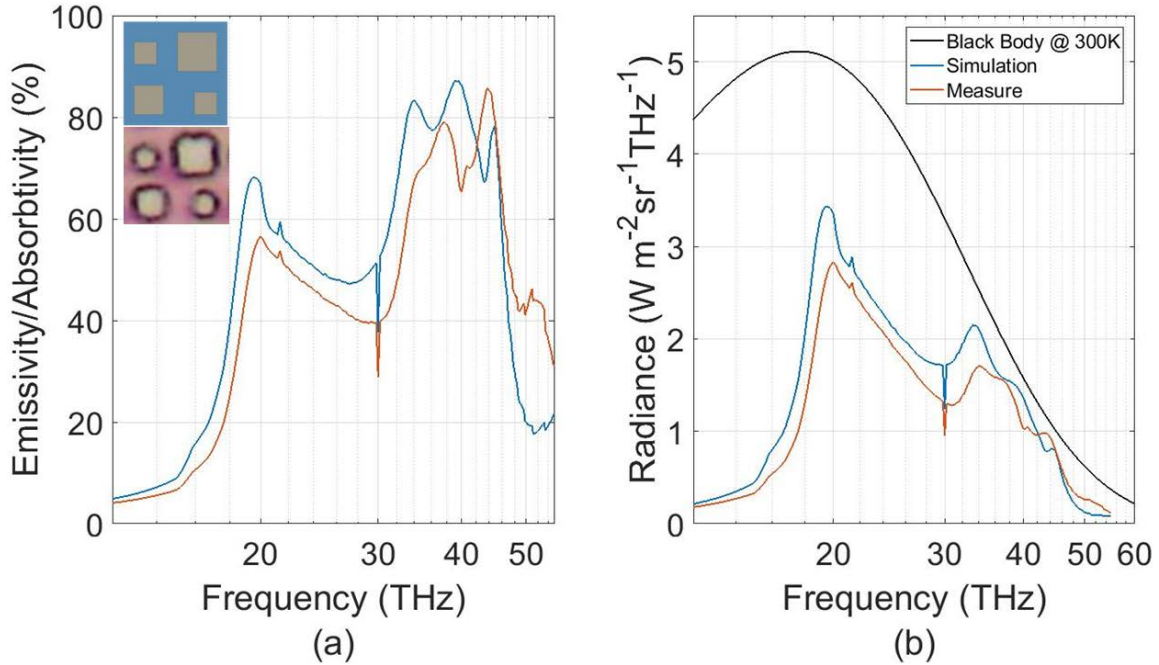


Figure shows (a) the emissivity/absorptivity and (b) the spectral radiance for the simulated optimized unit cell B geometry and the fabricated optimized unit cell B geometry. The top left corner of (a) shows a picture of the simulated unit cell and the fabricated unit cell.

Figure 38. Emissivity and Spectral Radiance of the Simulated and Fabricated Unit Cell B Geometry

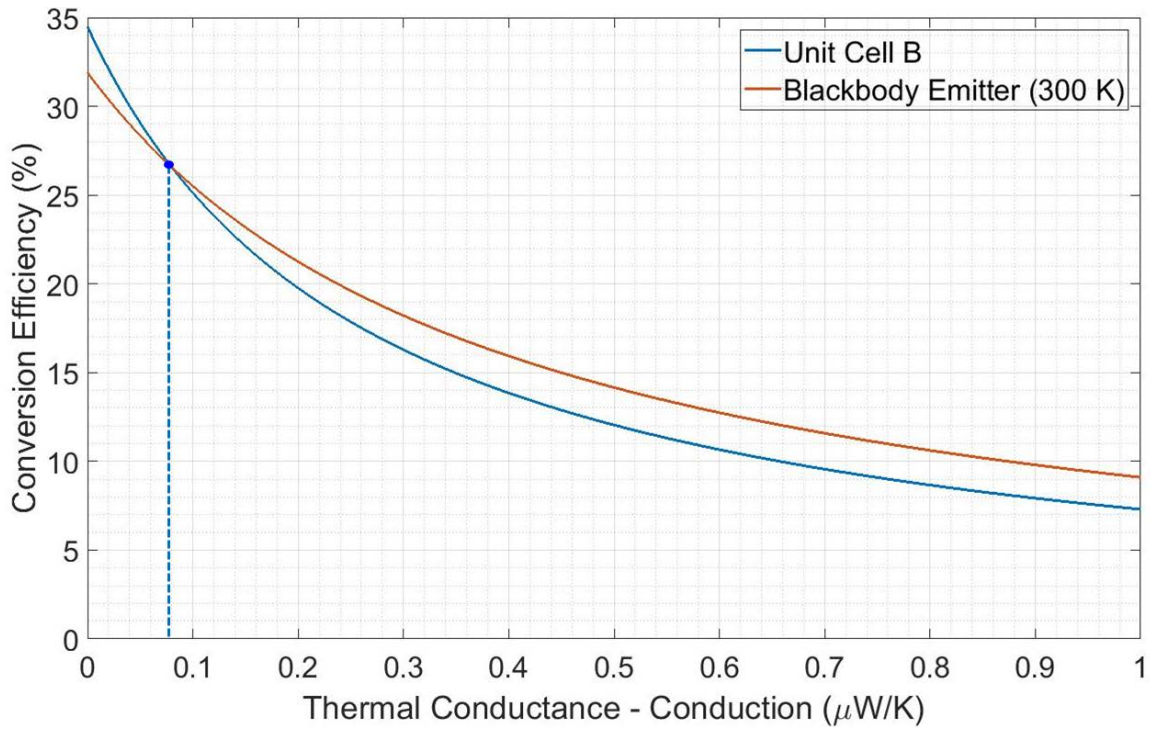
Table 5 outlines the summary of the results for unit cell A and B. For comparative purposes, the results of the fabricated sensor are included along with expected results if a blackbody was used, and an ideal emitter was used in place of the broad band IR emitter. It was assumed that the blackbody was on top of a thin, 300 nm, dielectric. For the ideal emitter, it was assumed to have a 300 nm dielectric and the emittance is one in the bandwidth of the camera and zero everywhere else. The ideal emitter was shown to illustrate the fundamental limit for this type of band converter. For all the sensors in Table 6, it was assumed a THz metamaterial absorber on the front side with an emittance shown in Figure 8.

Table 5. Summary of Results For Unit Cells A, B, and C

	Thermal Conductance [ $\mu\text{W/K}$ ]	Conversion Efficiency [%]	Speed Of operation [Hz]	In-Band Radiance [ $\text{W}/(\text{sr m}^2)$ ]	Total Radiance [ $\text{W}/(\text{sr m}^2)$ ]	Radiance Ratio [%]
Unit Cell A	0.85	8.1	1.2	46.6	54.0	86.3
Unit Cell B	0.85	8.4	1.6	48.9	60.0	81.5
Fabricated Sensor	1.10	6.5	1.6	46.9	80.5	58.3
Blackbody (300K)	0.70	11.6	1.8	66.3	146.0	45.9
Ideal Emitter	0.70	13.0	1.6	66.3	66.3	100

Summary of the results for unit cell A and B. Radiance ratio is the ratio of in-band radiance to total radiance of the broad band IR emitter. All sensors assume a THz metamaterial front-side with an emissivity shown in Figure 8. For comparison, results for the fabricated sensor and a black body sensor are included. The blackbody sensor assumes a THz metamaterial front-side and a black body used for the broad band IR emitter with a thin, 300 nm, dielectric. The ideal emitter represents the best case sensor with a dielectric thickness of 300 nm.

As it can be seen from Table 6, results did not vary much between the unit cells. Since all the unit cells used have about the same dielectric thickness, the thermal conductance did not vary significantly. Therefore, conversion efficiency was driven mostly by the radiance and the radiance ratio, which is the ratio of the in-band radiance to the total radiance. For the sensor configurations analyzed here, because the thermal conductance is large, the best performance is given by the black body. Using a blackbody as an emitter decreases the impact of the thermal conductance by increasing thermal losses through radiation and therefore increases the conversion efficiency. As thermal conductance decreases, thermal losses due to radiation would start to dominate the conversion efficiency. Figure 39 shows the conversion efficiency versus thermal conductance for unit cell B and a blackbody emitter, as outlined in Table 6. As shown in the figure, thermal conductance would need to be below  $0.8 \mu\text{W/K}$  in order for unit cell B to have a higher conversion efficiency than the blackbody emitter. As the emissivity of the emitter becomes close to ideal, the intersection point in Figure 39 would move to the right, making the use of the metamaterial more practical.



Plot comparing the conversion efficiency vs. thermal conductance of unit cell B and a sensor using a blackbody for an emitter. Both sensors assume a THz metamaterial absorber with emissivity shown in Figure 8. The blackbody emitter assumes an operating temperature of 300 K.

Figure 39. Conversion Efficiency of Unit Cell B vs. a Blackbody Emitter

## V. CONCLUSION

THz imaging continues to be a challenge that drives the research of novel sensing techniques. Using sensors that convert THz energy to IR showed a great potential to make real time THz imagers viable. Utilizing a THz-to-IR converter, will allow existing commercial thermal cameras to be used as a THz imager reducing complexity and cost while enhancing performance when compared with current schemes. Our sensor uses a double sided metamaterial to convert THz energy to IR. The front side of the sensor absorbs the incoming terahertz radiation and stores that energy as heat. The heat is isolated in individual pixels by thermal isolating beams. The backside of the sensor is a metamaterial emitter, tuned to emit IR radiation in the bandwidth of the IR camera.

This research focused on refining a design process of a broad-band IR emitter using a FE simulation model. Also, figures of merit were defined in order to help with the design process. Conversion efficiency and speed of operation were used to evaluate sensor performance for several broadband emitter geometries. It was found that speed of operation and conversion efficiency tends to play against each other. As conversion efficiency increases, this tends to decrease energy losses through thermal conduction and radiated energy outside the bandwidth of the IR camera. This will cause the pixel of the sensor to retain thermal energy longer and thereby decrease the frequency of operation. In order to increase the conversion frequency and speed of operation, IR radiation in the bandwidth of the camera must be increased. Conversion efficiency can also be increased by decreasing thermal conduction through the thermal isolating legs, but doing so would also decrease the frequency of operation.

Two metamaterial geometries were explored using a FE simulation using COMSOL. These simulations were compared to a previously fabricated sensor. The fabricated sensor utilizes the same THz tuned metamaterial for both the front-side and back-side of the sensor. The two broad band emitter geometries were also compared to a blackbody emitter and an ideal emitter. The results of these simulations led to the development of the following generalized conclusions:

1. Conversion efficiency increases as the ratio of in-band radiance to total radiance increases (as long as thermal conductance is comparatively low).
2. Decreasing thermal conductance increases conversion efficiency.
3. Frequency of operation increases as total radiance increases.
4. Frequency of operation increases as thermal capacity decreases ( from equation (10))
5. Generally, increasing dielectric thickness will increase total radiance.
6. Increasing dielectric thickness increases thermal capacitance.

These properties are coupled and difficult to be addressed separately without compromising the performance. They were used to define the process for designing a broadband IR emitter.

Because of thermal losses due to thermal conductance through the thermal isolating legs and lost thermal radiation from the front and back-side of the sensor, using a blackbody as an emitter could be a viable option, especially if it could be made utilizing a thin dielectric. Using a blackbody would decrease the significance of thermal conducting losses.

Another potential way to improve efficiency would be to increase the temperature of operation of the sensor. Examining the equations that govern the thermodynamics of the THz-to-IR converter, (2), (5), (6), and (10), this fact becomes evident. This should also be explored in future work.

In order to improve conversion efficiency and frequency of operation, other metamaterial geometries and material will need to be explored. It might be worth exploring different geometries and materials that are closer to blackbodies. Materials with a low thermal conductance and thermal capacitance will also decrease thermal conductance and therefore improve conversion efficiency.

Using the data presented in this thesis SRL can continue refining the FE simulation to aid in the design process. The data will also help SRL in making an educated decision in the pursuit of a suitable broadband IR emitter to be used in the sensor.

THIS PAGE INTENTIONALLY LEFT BLANK

## LIST OF REFERENCES

- [1] H. Tao, E. A. Kadlec, A. C. Strikwerda, K. Fan, W. J. Padilla, R. D. Averitt, E. A. Shaner and X. Zhang, “Microwave and Terahertz wave sensing with,” *Optics Express*, vol. 19, no. 22, 2011.
- [2] F. Alves, G. Karunasiri, N. V. Lavrik and D. Grbovic, “Bi-material terahertz sensors using metamaterial structures,” *Optics Express*, vol. 21, no. 11, 2013.
- [3] Behnken, B. N., Karunasiri, G., Chamberlin, D. R., Robrish, P. R., Faist, J. “Real-time imaging using a 2.8 THz quantum cascade laser and uncooled infrared microbolometer camera.” *Opt. Lett.*, vol. 33, pp. 440–442, 2008.
- [4] S. A. Kuznetsov, A. G. Paulish, A. V. Gelfand, P. A. Lazorskiy and V. N. Fedorinin, “Bolometric THz-to-IR converter for terahertz imaging,” vol. 99, no. 2, 2011.
- [5] Lowe, M. “Imaging of 3.4 THz quantum cascade laser beam using uncooled microbolometer camera.” M.S. thesis, Dept. App Physics, Naval Postgraduate School, Monterey, CA, Dec. 2006.
- [6] F. Alves, B. Kearney, D. Grbovic, N. V. Lavrik, and G. Karunasiri, “Strong terahertz absorption using SiO<sub>2</sub>/Al based metamaterial structures,” *Appl. Phys. Lett.*, vol. 100, 2012.
- [7] F. Alves, D. Grbovic and G. Karunasiri, “Investigation of microelectromechanical systems bi-material sensors with metamaterial absorbers for terahertz imaging,” *Optical Engineering*, vol. 53, no. 9, 2014.
- [8] F. Alves, D. Grbovic, B. Kearney, and G. Karunasiri, “Microelectromechanical systems bimaterial terahertz sensor with integrated metamaterial absorber,” *Opt. Lett.*, vol. 37, pp. 1886–1888, Jun. 2012.
- [9] F. Alves, D. Grbovic, B. Kearney, and G. Karunasiri, “High sensitivity metamaterial based bi-material terahertz sensor,” in *Proc. SPIE*, vol. 8624, 2013, pp. 862411–862419.
- [10] F. Alves, L. Pimental, D. Grbovic and G. Karunasiri, “MEMs terahertz-to-infrared band converter using frequency selective planar metamaterial,” *Scientific Reports* Aug. 2018.
- [11] Ashmore, J. “MEMS terahertz focal plane array for use with infrared imaging systems.” M.S Thesis, Dept. App Physics, Naval Postgraduate School, Monterey, CA, Jun. 2017.

- [12] H. Gonzalez, “MEMS terahertz focal plane array with optical readout,” M.S. Thesis, Dept. App. Physics, Naval Postgraduate School, Monterey, CA, Jun. 2016.
- [13] *User’s manual FLIR T10xx series*. FLIR systems, Inc, Wilsonville, OR, 2016.
- [14] *User’s manual ResearchIR 4*. FLIR systems, Inc, Wilsonville, OR, 2015 .
- [15] *User’s Manual for EasyQCL-1000*. LongWave Photonics LLC, San Leandro, CA, 2015, pp. 1–8.
- [16] F. Alves, B. Kearney, D. Grbovic and G. Karunasiri, “Narrowband terahertz emitters using metamaterial films,” *Optics Express*, vol. 20, no. 21, 2012.
- [17] C. Gong, M. Zhan, J. Yang, Z. Wang, H. Liu, Y. Zhoa and W. Liu, “Broadband terahertz metamaterial absorber based on sectional asymmetric structures,” *Scientific Reports*, vol. 10, no. 32, 2011.
- [18] M. Polyanskiy, “RefractiveIndex.info,” 2008–2018. [Online]. Available: <https://refractiveindex.info>. [Accessed 31 July 2018].

## **INITIAL DISTRIBUTION LIST**

1. Defense Technical Information Center  
Ft. Belvoir, Virginia
2. Dudley Knox Library  
Naval Postgraduate School  
Monterey, California